The Astrophysical Journal, 837:51 (17pp), 2017 March 1 https://doi.org/10.3847/1538-4357/aa5f56

Mass Distribution in Galaxy Cluster Cores

M. T. Hogan[1,2], B. R. McNamara[1,2], F. Pulido[1], P. E. J. Nulsen[3,4], H. R. Russell[5], A. N. Vantyghem[1], A. C. Edge[6], and R. A. Main[7]
[1] Department of Physics and Astronomy, University of Waterloo, Waterloo, ON, N2L 3G1, Canada; m4hogan@uwaterloo.ca
[2] Perimeter Institute for Theoretical Physics, Waterloo, ON, N2L 2Y5, Canada
[3] Harvard-Smithsonian Center for Astrophysics, 60 Garden Street, Cambridge, MA 02138, USA
[4] ICRAR, University of Western Australia, 35 Stirling Hwy, Crawley, WA 6009, Australia
[5] Institute of Astronomy, Madingley Road, Cambridge CB3 0HA, UK
[6] Centre for Extragalactic Astronomy, Department of Physics, Durham University, Durham DH1 3LE, UK
[7] Canadian Institute for Theoretical Astrophysics, University of Toronto, 60 St. George Street, Toronto, ON, M5S 3H8, Canada
Received 2016 October 4; revised 2017 January 30; accepted 2017 February 4; published 2017 March 2

Abstract

Many processes within galaxy clusters, such as those believed to govern the onset of thermally unstable cooling and active galactic nucleus feedback, are dependent upon local dynamical timescales. However, accurate mapping of the mass distribution within individual clusters is challenging, particularly toward cluster centers where the total mass budget has substantial radially dependent contributions from the stellar (M_*), gas ($M_{\rm gas}$), and dark matter ($M_{\rm DM}$) components. In this paper we use a small sample of galaxy clusters with deep *Chandra* observations and good ancillary tracers of their gravitating mass at both large and small radii to develop a method for determining mass profiles that span a wide radial range and extend down into the central galaxy. We also consider potential observational pitfalls in understanding cooling in hot cluster atmospheres, and find tentative evidence for a relationship between the radial extent of cooling X-ray gas and nebular Hα emission in cool-core clusters. At large radii the entropy profiles of our clusters agree with the baseline power law of $K \propto r^{1.1}$ expected from gravity alone. At smaller radii our entropy profiles become shallower but continue with a power law of the form $K \propto r^{0.67}$ down to our resolution limit. Among this small sample of cool-core clusters we therefore find no support for the existence of a central flat "entropy floor."

Key words: galaxies: clusters: general – galaxies: clusters: intracluster medium – galaxies: elliptical and lenticular, cD – galaxies: kinematics and dynamics

1. Introduction

Galaxy clusters constitute the peaks of the large-scale structure of the universe, and as such are invaluable cosmological probes (for a review see Allen et al. 2011). Furthermore, individual clusters are sizable enough to encompass a representative universal volume, making them ideal natural laboratories in which to study physical processes ranging from galaxy evolution through to gas dynamics, feedback from active galactic nuclei (AGNs), and beyond. Knowledge of the total mass and its distribution within each cluster is vital, since the cluster mass function is a critical test of cosmological models while many of the internal workings of clusters are tuned to the local acceleration.

Recently the *Hitomi* satellite (Takahashi et al. 2010; Kitayama et al. 2014) observed the central regions ($\lesssim$60 kpc) of the Perseus cluster (Hitomi Collaboration et al. 2016), finding remarkably low levels of turbulence in its intracluster medium (ICM). These data showed the turbulent pressure contribution to be only about 4% of the thermal support. The core of Perseus is a highly active feedback system harbouring cavities, shocks, and sound waves (Fabian et al. 2000, 2003; Sanders & Fabian 2007). It had been suggested that such intense nuclear activity may raise ICM turbulence (Churazov et al. 2001), potentially biasing X-ray cluster mass estimates low (e.g., Nagai et al. 2007). The *Hitomi* result therefore suggests that techniques assuming hydrostatic equilibrium are reasonable for measuring masses on relatively small scales even in active environments. This is supported by earlier work showing that turbulent motions are likely suppressed at the centers of giant ellipticals (Werner et al. 2009). The caveat that *Hitomi* was only able to observe a single cluster before its unfortunately premature demise (see Witze 2016) should of course be considered (Blanton 2016). Similarly, other sources of nonthermal pressure such as cosmic rays are known to be present in clusters (e.g., Boehringer & Morfill 1988; Kravtsov & Borgani 2012; Nelson et al. 2014, and references therein). Nevertheless, deep grating observations suggest that modest nonthermal support (<20%) appears common in relaxed clusters (Sanders & Fabian 2011). Low turbulence ($\lesssim$25%) is also seen in at least some isolated ellipticals (e.g., Werner et al. 2009; Churazov et al. 2010), although the turbulent contribution could be higher in more disturbed galaxies (de Plaa et al. 2012).

Cluster mass profiles on various scales are calculated using a variety of techniques; for example using X-ray data (e.g., Vikhlinin et al. 2006; Allen et al. 2008; Main et al. 2015), weak lensing (e.g., Kubo et al. 2009; Hoekstra et al. 2013, 2015), the Sunyaev–Zel'dovich effect (e.g., Plagge et al. 2010; Bleem et al. 2015; Planck Collaboration et al. 2015), galaxy motions (e.g., Wojtak & Łokas 2010), and stellar velocity dispersions (Fisher et al. 1995; Lauer et al. 2014). However, each technique has its limitations (see, e.g., discussions in Mandelbaum 2015; Biffi et al. 2016), and we note in particular that hydrostatic mass estimates at $\lesssim$10 kpc are possible for only the most local clusters (e.g., M87, see Romanowsky & Kochanek 2001; Russell et al. 2015). In this paper we use a small set of clusters whose mass profiles have prior comparisons available at both small and large clustercentric radii to develop a technique to determine cluster mass profiles across wide radial ranges. The techniques described will be applied to a larger sample of clusters in upcoming papers to investigate the mass dependence

of AGN feedback and thermal instability in clusters more generally.

A major facet in the quest to fully understand galaxy clusters is determining the processes that maintain the long-term state of settled systems. Without a heating mechanism, the hot ICM of an isolated cluster should cool at a rate of between about one hundred and several thousand $M_{\odot}\,\mathrm{yr}^{-1}$(i.e., the "classical cooling flow," see Fabian 1994). However, a deficit of cooling gas at intermediate temperatures (Peterson et al. 2003; Sanders & Fabian 2011) coupled to much lower than predicted levels of molecular gas (e.g., Edge 2001; Salomé & Combes 2003) and star formation (O'Dea et al. 2008; Rafferty et al. 2008) in cluster centers belies this classical model. The implication is that some mechanism is retarding the predicted cooling. In the standard picture, radio-mechanical feedback from AGN jets hosted by the central brightest cluster galaxy (BCG) provides the required energy by inflating cavities in the X-ray atmosphere, which rise buoyantly and subsequently drive turbulence, weak shocks, and sound waves. Exactly how this feedback energy couples to the ICM is unclear (see review by Soker 2016), with recent work suggesting that gas mixing may be the dominant heating mechanism alongside contributions from turbulence and shock heating (Hillel & Soker 2016a, 2016b; Yang & Reynolds 2016). Indeed the relative importance of these mechanisms may change during episodes of AGN activity (Li et al. 2015), though the time-averaged energy output of the AGN is more than sufficient to counteract the expected ICM cooling (see McNamara & Nulsen 2007, 2012; Fabian 2012 for reviews). Nevertheless, residual cooling must occur within clusters to explain the observed cold gas, ongoing star formation, and extended envelopes of multiphase gas seen surrounding BCGs (e.g., Edge 2001; Salomé & Combes 2003; McDonald et al. 2010; Tremblay et al. 2015) in these so-called "cool-core" clusters.

Central to understanding this feedback cycle is determining the physical triggers that initiate transitions between periods of increased heating and cooling. It has been shown that multiphase gas and increased star formation are preferentially observed in cluster cores when the central entropy parameter K_0 drops below $30\,\mathrm{keV\,cm}^2$ (Cavagnolo et al. 2008; Rafferty et al. 2008; Sanderson et al. 2009), or equivalently the central cooling time t_{cool} drops below 5×10^8 yr. However, outliers show that additional physics is required beyond these simple binary indicators. An intriguing possibility that has recently gained support from both simulations (e.g., McCourt et al. 2012; Sharma et al. 2012; Li et al. 2015) and observations (Voit & Donahue 2015; Voit et al. 2015) is that the hot gas becomes thermally unstable when the minimum ratio of its cooling time to free-fall time ($t_{\mathrm{cool}}/t_{\mathrm{ff}}$) falls below a certain value, reported to be approximately 10. In these "precipitation models," condensation of hot gas ensues once this cooling threshold has been breached. Alternatively, motivated by low molecular cloud velocities observed by ALMA (McNamara et al. 2014; Russell et al. 2014, 2016; Vantyghem et al. 2016), McNamara et al. (2016) proposed a model of "stimulated feedback" in which partially cooled gas from cluster cores is triggered to condense by being lifted in the wake of X-ray cavities to an altitude at which its ratio of cooling time to infall time $t_{\mathrm{cool}}/t_{\mathrm{I}}$ falls below some threshold (see also Voit et al. 2016). Both these models vitally depend on dynamical timescales that require robust cluster mass profiles. Being able to test these models in order to further our understanding of the feedback cycle within galaxy clusters therefore serves as the major motivation for this work.

The paper is arranged as follows. In Section 2 we describe our sample and data reduction. In Section 3 we investigate the cooling properties of the gas within these clusters. Section 4 uses mass tracers at a variety of wavelengths to develop a method for determining mass profiles that is applicable to less well studied clusters and discusses properties that can affect, or be affected by, these mass distributions. Section 5 makes some final remarks, before conclusions are given in Section 6. In this paper we have assumed a standard ΛCDM cosmology with: $\Omega_{\mathrm{m}}=0.3$, $\Omega_{\Lambda}=0.7$, and $H_0=70\,\mathrm{km\,s^{-1}\,Mpc^{-1}}$.

2. Sample and Data Reduction

2.1. Sample Selection

One motivation for our work is to develop a technique to calculate cluster mass profiles in order to study the relevance of the $t_{\mathrm{cool}}/t_{\mathrm{ff}}$ threshold to the onset and magnitude of ICM cooling from the hot phase in cool-core clusters. The techniques described herein are to be applied to a larger sample to study this threshold using more powerful statistical tests in upcoming papers. For now, the aim is to develop the techniques on a smaller selection of well-studied objects where comparison checks to their mass profiles, particularly at small radii, are possible.

We select the four clusters (A2029, A2199, A496, A85) for which Fisher et al. (1995) measured velocity dispersion profiles across a range of radii, and that have >100 ks archival *Chandra* data. These velocity dispersions allow a comparison to the inner mass profiles. All four of these clusters were included in the sample of Main et al. (2015), who derived total mass estimates for them. A2029 has additional X-ray-derived total mass estimates from Allen et al. (2008) and Vikhlinin et al. (2006), whereas A2029, A2199, and A85 have weak-lensing mass estimates available (Cypriano et al. 2004; Kubo et al. 2009). To these four we add the Hydra A cluster,[8] which has dynamical mass constraints at small radii from Hamer et al. (2014) in addition to X-ray and weak-lensing mass estimates at larger radii (Okabe et al. 2015).

Each of these clusters has a central cooling time less than 1×10^9 yr (Cavagnolo et al. 2009). All have been observed for the presence of Hα emission, with detections in all but A2029 (Crawford et al. 1999; McDonald et al. 2010), as well as having had measurements taken of their molecular gas content (Edge 2001; Salomé & Combes 2003).

2.2. Data Reduction

Archival *Chandra* imaging data for our sample clusters were downloaded from the online repository. Data were reduced using CIAO version 4.7, with CALDB version 4.6.7 (Fruscione et al. 2006). Level-1 events were reprocessed to correct for charge transfer inefficiencies (CTIs) and time-dependent gains. The events were filtered to remove bad grades, with VFAINT filtering used when this mode was on. Background light curves were extracted from level-2 events files on a complementary chip to the one that contained the bulk of the cluster emission.

[8] We hereafter refer to this cluster as "Hydra A," although note that this name is also used in the literature to refer only to the central radio source and/or BCG. This cluster is also often erroneously referred to as A780 in the literature —that cluster is actually a background source with no physical connection to Hydra A. Note that "Hydra A" is distinct from the "Hydra Cluster" (A1060).

Table 1
Chandra Data Used in our Analysis

Cluster	z	Scale (kpc arcsecond^{-1})	Observation IDs	Total Exposure (ks)		N_H (10^{22} cm^{-2})	Cluster Center	
				Raw	Cleaned		R.A. (J2000)	Decl. (J2000)
A2029	0.0773	1.464	891, 4977, 6101	107.63	103.31	0.033	15:10:56.077	+05:44:41.05
A2199	0.0302	0.605	10748, 10803, 10804, 10805	119.87	119.61	0.039	16:28:38.245	+39:33:04.21
A496	0.0329	0.656	931, 3361[a], 4976	104.00	62.75	0.040	04:33:37.932	−13:15:40.59
A85	0.0551	1.071	904, 15173, 15174, 16263, 16264	195.24	193.64	0.039	00:41:50.476	−09:18:11.82
Hydra A	0.0550	1.069	4969, 4970	195.74	163.79	0.043	09:18:05.681	−12:05:43.51

Notes. Given scales are the angular scale on the sky at the given redshifts using standard cosmology.
[a] This observation was completely affected by a large flare and removed from analysis.

These light curves were filtered using the LC_CLEAN script provided by M. Markevitch, to remove time periods affected by background flares.

For sources with multiple observations, the reprocessed events files were reprojected to the coordinates of the observation ID (OBSID) with the longest exposure. Blank-sky backgrounds were extracted for each observation and processed identically to the target files, reprojected to the corresponding position, and normalized to match the 9.5–12.0 keV flux of each observation. Images were created in the energy range 0.5–7.0 keV for each OBSID. For the purposes of identifying point sources and structure in the ICM, these images were summed and background-subtracted for each source. A map of the point-spread function (PSF) was created from the OBSID with the longest exposure for each object. In conjunction with using this PSF map to correct for PSF degradation away from the pointing center, the WAVDETECT algorithm (Freeman et al. 2002) of CIAO was used to detect point sources in each of these summed images. These point sources were inspected, and where necessary corrected, in DS9 before being masked out from subsequent analysis. We similarly masked clear structures within the ICM such as cavities and filaments, since these regions are typically out of equilibrium and their inclusion could bias derived properties.

2.2.1. Spectral Extraction

The cooling instabilities we aim to study typically occur at small ($\lesssim$10 kpc) radii and so we desire finely binned spectra in the central cluster regions. The example clusters in this preliminary investigation were purposefully chosen to have deep *Chandra* data, hence our choice of annuli from which to extract spectra is effectively limited by resolution rather than number of counts.

Concentric circular annuli were defined for each cluster, centered at the positions given in Table 1 (see Section 4.6 for cluster centering considerations). The central annulus is given a width of just 3 pixels (roughly equivalent to the maximal angular resolution of *Chandra*), where each pixel is 0.492 arcsec across. Successive annuli are given widths that increase by 1 pixel each until the sixth annulus, beyond which we make the width of each annulus 1.5 times the width of the preceding one until we reach ∼1400 pixels, giving a total of 16 annuli per source. This sampling ensures that we have 3–6 annuli with radii <10 kpc, that our central annulus is at the resolution limit of *Chandra* and contains >3000 net counts, and that we can trace the resulting profiles to large radii. The geometric increase in annular size means that the number of counts in each successive annulus increases, which was found to ensure more successful deprojection (see Section 3.2).

Spectra were extracted separately from each OBSID. Individual response matrix files and auxiliary response files were created for each, using MKACISRMF and MKWARF respectively, and the spectra were grouped to a minimum of 30 counts per channel. The multiple observations for a given source can be separated substantially in time, hence we chose not to sum the spectra, instead keeping them separate and later loading and fitting simultaneously within XSPEC. Exposure maps were created for each observation and used to correct for area lost to point sources, chip gaps, etc.

3. Cluster Properties

3.1. Projected Profiles

The extracted spectra for each cluster, alongside their matched response files, were loaded into XSPEC version 12.8.2 (Arnaud 1996). To derive the projected gas properties of these clusters we initially fitted an absorbed single-temperature (PHABS*MEKAL) model (Mewe et al. 1985, 1986; Balucinska-Church & McCammon 1992; Liedahl et al. 1995). Extracted spectra for all OBSIDs within each annulus were fitted simultaneously. Our starting values for line-of-sight galactic absorptions were taken from the LAB Survey (Kalberla et al. 2005)—our fitting suggested higher values were required for A2199 and A85, in agreement with the findings of Main et al. (2015), hence we adopted the N_H values of these latter authors and subsequently kept these parameters frozen in our analysis (see Table 1). Metallicity was allowed to vary in each bin as a free parameter.

The outputted temperature and normalization (N) parameters from our fitted models were used to derive the projected number densities

$$n_e = D_A(1+z)10^7\sqrt{\frac{N\ 4\ \pi\ 1.2}{V}} \quad (1)$$

where the factor of 1.2 comes from the ionization ratio n_e/n_p. In turn, these parameters were used to derive profiles of pressure ($P = 2n_e\,kT$) and entropy ($K = kT\ n_e^{-2/3}$). Cooling times were calculated assuming compressionless thermal cooling, using the relation

$$t_{cool} = \frac{3\ P}{2\ n_e\ n_H\ \Lambda(Z,\ T)} \quad (2)$$

where P is pressure, and n_e and n_H are electron and hydrogen number densities respectively. $\Lambda(Z,\ T)$ is the cooling function for gas at a specific abundance and temperature. Practically this relation can be simplified to $3\ P\ V/2\ \mathcal{L}_X$ where V is the volume $\frac{4}{3}\pi\,(r_{out}^3 - r_{in}^3)$ bounded by the projected edges of each annulus,

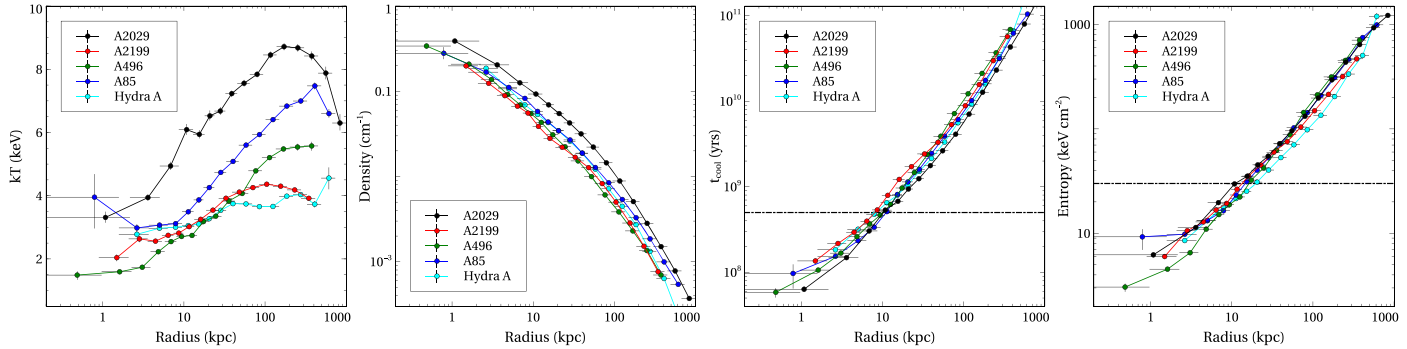

(a) Temperature (b) Density (c) Cooling time (d) Entropy

Figure 1. Projected temperature, density, cooling time (t_{cool}), and entropy profiles. The dotted horizontal lines in panels (c) and (d) show the thresholds for cooling time of 5×10^8 yr and for entropy of 30 keV cm^2, respectively. Note that all sources satisfy both thresholds (see Section 3.1). Regardless of this and unlike the other four sources shown here, A2029 does not display nebular emission indicative of ongoing cooling.

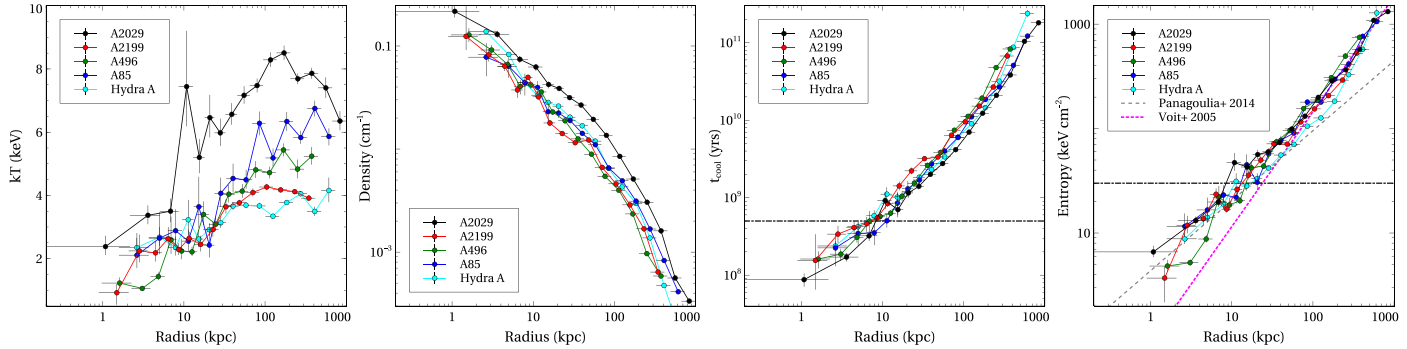

(a) Temperature (b) Density (c) Cooling time (d) Entropy

Figure 2. Fully deprojected temperature, density, cooling time (t_{cool}), and entropy profiles. The dotted horizontal lines in panels (c) and (d) show the thresholds for cooling time of 5×10^8 yr and for entropy of 30 keV cm^2, respectively. Note that all sources satisfy both thresholds, as was the case for the projected profiles (see Figure 1). In panel (d) we show the overall best fitting power-law model to the inner entropy profiles of a sample of 66 nearby clusters presented by Panagoulia et al. (2014) and a standard cluster entropy profile with scaling $K \propto r^{1.1}$ as expected from gravity alone (e.g., Tozzi & Norman 2001; Voit et al. 2005). Note that the normalization of this latter power law is adjusted to match our profiles.

and $\mathcal{L}_X$ its bolometric X-ray luminosity, which we obtain by integrating the unabsorbed thermal model between 0.1 and 100 keV. We plot the projected temperature, density, t_{cool}, and entropy profiles of our five clusters in Figure 1. Note that the central annulus of both Hydra A and A2199 was removed because the emission is dominated by a nonthermal point source associated with their respective AGNs.

Of the five clusters studied here only A2029 does not display nebular emission indicative of ongoing cooling, down to an Hα flux limit of $F_{H\alpha} < 3 \times 10^{-16}$ erg s^{-1} cm^{-2} (Crawford et al. 1999; McDonald et al. 2010). In Figure 1 we see that this cluster has a comparatively higher temperature and density, although note that all five of the clusters satisfy the thresholds for central cooling time in projection. Comparison to the threshold for central entropy parameter $K_0 < 30$ keV cm^2 of Cavagnolo et al. (2008) is less straightforward. The fitting formula used to derive this threshold is $K(r) = K_0 + K_{100}(r/100\,\mathrm{kpc})^{\alpha}$ (Donahue et al. 2006; Cavagnolo et al. 2008, 2009). The parameter K_0 is therefore the difference between the entropy profile at small radii and an extrapolation of the (typically steeper) entropy profile at large radii. For non-cool-core clusters with very high central entropy, K_0 is equivalent to the central entropy to a good approximation. For cool-core clusters (which our sample consists of) with low central entropies this approximation is no longer valid. However, since the extrapolation of the high-altitude entropy profile cannot drop below zero this makes the measured inner value a hard upper limit to K_0 such that if $K < 30$ keV cm^2 then K_0 must be below the threshold. All of our measured central entropies drop below this cutoff, hence all of our profiles satisfy the threshold for the central entropy parameter.

3.2. Deprojected Profiles

Measured central properties of galaxy clusters can be significantly affected by emission from hotter regions at higher altitude contaminating the central spectra in projection. To derive more accurate profiles therefore requires us to deproject our spectra, which we perform using the model-independent DSDEPROJ routine (Russell et al. 2008, also see Sanders & Fabian 2007, 2008). Through various trials we found that ensuring both the radius and counts enclosed increased from each inner annulus to the next one out provided the most robust deprojections.

We again fitted an absorbed single-temperature PHABS*MEKAL model to these deprojected spectra and used the fitted quantities to derive the deprojected density, cooling time, and entropy profiles that are shown in Figure 2. Fits failed in the central annulus due to the low number of counts left after deprojection for all sources except A2029, whose central bin contains a physically larger region due to its higher redshift. The lower central densities derived after deprojection increased the central ($\lesssim$5 kpc) cooling times by $\sim$15%–50%, and the central entropies by $\sim$5%–20%. All sources still satisfy the

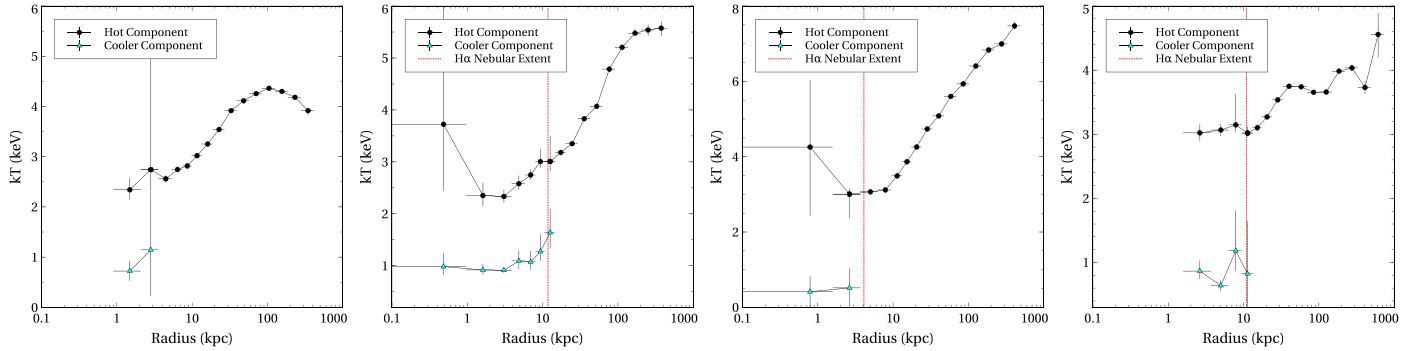

(a) A2199 (b) A496 (c) A85 (d) Hydra A

Figure 3. Projected two-temperature fits showing the presence of a cooler component toward the center of four of our clusters. Shown in red is the radial extent of the Hα nebular emission reported by McDonald et al. (2010). A2029 showed no requirement for a second temperature component, hence its omission here. Note that these temperature measurements are likely overestimated—the resulting counts after deprojection meant that two-temperature models could only be successfully fitted for the projected spectra. Nevertheless, cooling gas is recovered in all systems with known Hα. Furthermore there is tentative evidence for a relation between the extent of Hα and that of the cooler X-ray component.

thresholds for central entropy and cooling time after deprojection. We note that A2029 has a higher temperature than the other clusters shown here, but that its correspondingly higher density ensures that it meets the cooling criteria.

3.2.1. Lack of an "Entropy Floor"

The entropy profile is a powerful diagnostic for understanding the ICM because it effectively encodes the thermal history of the cluster. A baseline power-law entropy profile with scaling $K \propto r^{1.1}$ is expected from gravity alone (e.g., Tozzi & Norman 2001; Voit et al. 2005). We plot a power law with this index and a normalization adjusted to match our profiles in Figure 2(d), finding that it gives a good approximation to our entropy profiles at large radii ($\gtrsim$50 kpc). Deviations from this index therefore give a measure of the impact of nongravitational processes. Panagoulia et al. (2014) fitted a power-law model to the deprojected inner entropy profiles of a sample of 66 nearby ($z < 0.071$) clusters. In Figure 2(d) we plot the best fitting power-law model of Panagoulia et al., $K = 95.4 \times (r/100\,\mathrm{kpc})^{0.67}$. These authors found no evidence for flat entropy cores among the clusters in their sample (sometimes called an "entropy floor"—though this term is used with various definitions in the literature) as has been claimed elsewhere (e.g., David et al. 1996, 2001; Ponman et al. 2003; Cavagnolo et al. 2009), and suggest that such an effect may be due to resolution. Our inner entropy profiles agree well with this power law and similarly do not appear to flatten out, continuing to fall down to our resolution limit, thus ruling out the presence of large isentropic cores in these systems.

3.3. Two-temperature Fits

The centers of galaxy clusters often contain multi-temperature X-ray gas (e.g., Sanders & Fabian 2002; Panagoulia et al. 2013; Vantyghem et al. 2014; Russell et al. 2015). To test for this cooling indicator we refitted our clusters with a two-temperature model—PHABS*(MEKAL + MEKAL). Applying an F-test, we find that the fits at all radii disfavor the presence of a second temperature component in the ICM of A2029, consistent with the lack of other cooling tracers seen in this system (Edge 2001; Salomé & Combes 2003; Rafferty et al. 2008; McDonald et al. 2010). For the remaining four clusters we find that two-temperature models are favored in the inner regions when fitting to the projected profiles, though the extent of the two-temperature region is different for each of the four clusters.

The two-component temperature profiles are shown in Figure 3. Deprojected spectra contained too few counts (<8000 in all cases) to yield successful two-temperature fits. This lack of counts is amplified toward the center (typically <500 deprojected counts in the central bin), hence the annuli where the strongest two-temperature signal is expected are those that suffer from the lowest number of counts. Nevertheless, our projected fits show that a two-temperature ICM is present in all four clusters that we expect to be cooling, though we caution that the temperatures shown in Figure 3 are likely overestimated due to projection.

McDonald et al. (2010) used the Maryland Magellan Tunable Filter to detect and, where relevant, map the spatial distribution of Hα nebular emission in a sample of 23 cool-core clusters. Interestingly we find that in the three of our clusters present in McDonald et al. (2010) the radial extent of the Hα nebula matches the radius to which our fits favor a cooler component within the ICM (see Figure 3). This supports direct cooling from the hot phase as the source of the nebular gas. Similar spatial correlation between softer X-ray and emission-line nebulae has previously been observed in a small number of objects such as M87 (Sparks et al. 2004; Werner et al. 2013) and A426/Perseus (Fabian et al. 2003), as well as in 3D hydrodynamical simulations of condensing atmospheres (Gaspari et al. 2016). However, our small sample precludes any strong conclusions being drawn here and we leave further investigation of this to future study with an extended sample.

Importantly, we find that the temperature of the hotter component agrees with that recovered from the single-temperature model for radii >1 kpc. Since the hotter component is volume-filling, and we are most interested in the triggering of hydrostatic cooling from this phase, we can calculate cooling profiles of this hotter gas component in a similar fashion to that described in Section 3.1. For each cluster, the profile derived from the hotter component is in good agreement with that derived from a single-temperature fit down to our smallest radii. Furthermore, although the ratios of the normalizations between the hot and colder gas phases span a relatively wide range, they typically fall within ~10–60, showing that the colder component is significantly less

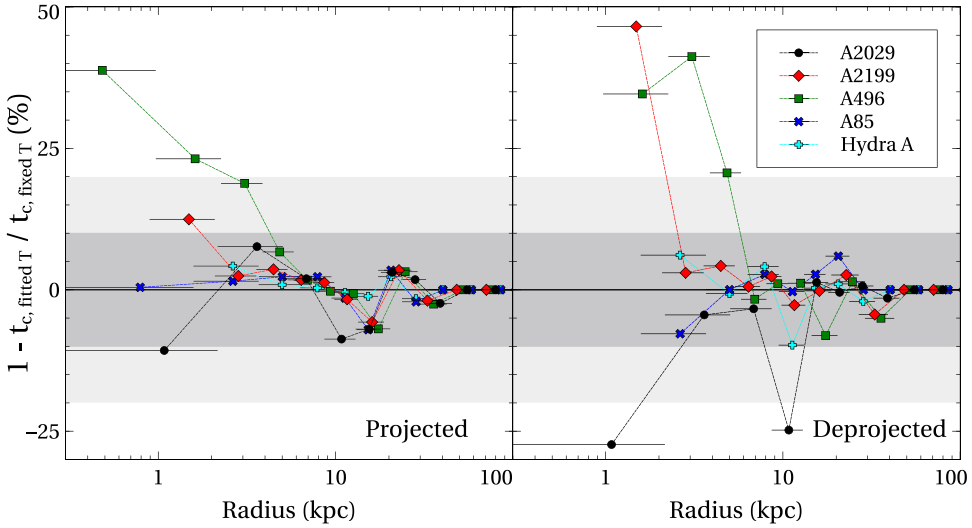

Figure 4. Percentage error introduced to resulting projected (left) and deprojected (right) cooling time profiles when a single temperature is assumed across the central ∼20 kpc, achieved here by first fitting to coarsely binned spectra and then forcing the resulting temperatures on the more finely binned spectra (see text for more details). Errors are typically <10% in projection, though the effect is exacerbated after deprojection.

abundant ($\lesssim$100×) than the hotter component (see also Section 3.4.1).

Studying NGC 4696 (Centaurus cluster's BCG) Panagoulia et al. (2014) found that the presence of a cooler component can suggest flattening in the entropy profile if not fully accounted for. However, this effect seems to be present only on physical scales $\lesssim$1 kpc in Centaurus and does not appear to flatten our single-temperature entropy profiles (Figure 2). Since scales <1 kpc are accessible only in the most nearby systems (see Russell et al. 2015), single-temperature fits are deemed adequate to trace cluster cooling profiles on the scales of interest to our study (see also Section 3.4.1).

3.4. Resolution Effects

The clustercentric radius where $t_{\rm cool}/t_{\rm ff}$ reaches its minimum, typically $\lesssim$20 kpc (Gaspari et al. 2012; Voit & Donahue 2015; Voit et al. 2015), is not well resolved in many clusters. This leads to a variety of effects that can limit the accuracy to which central cluster properties can be measured. The simplest of these effects is merely redshift-related—the fixed angular resolution of *Chandra* places an observational lower limit on the diameter of the innermost annulus, which contains a progressively larger physical volume of cluster core with increasing redshift. This can bias high the innermost measured temperatures of more distant clusters because the innermost spectrum encompasses typically hotter ICM emission from further out. Such an effect is unavoidable but must be considered when investigating cooling times among a sample of clusters that span a range in redshift.

Another effect that we can attempt to understand here is related to the number of counts required to successfully model the temperature and density of a portion of ICM. While densities can be reliably determined with only a few hundred counts, a robust single-temperature measurement typically requires at least 3000, depending on cluster temperature—hotter clusters require more counts. Oftentimes this can mean that only a single-temperature measurement is possible at $\lesssim$20 kpc, whereas the density profile alone could be measured to much smaller radii. Determination of the cooling time requires both of these parameters, which leaves an open decision. Authors can choose to truncate their cooling profiles at the radius required for parallel measurement of temperature and density, can attempt to model and extrapolate the temperature to the inner regions, or can calculate a cooling time profile to smaller radii by using the fitted densities coupled with a constant fixed central temperature. This choice can clearly affect the minimum cooling time.

The extent to which the latter resolution effect ultimately affects cooling times can be investigated by extracting more coarsely binned spectra. For each of our clusters we extract a single spectrum covering the same region as the innermost few original annuli, such that the central bin extends to an altitude of 18–20 kpc in each case. We set our second annulus to match the next couple of finely binned regions such that it covers the range ∼20–40 kpc, beyond which we revert to using identical regions to those defined in Section 2.2.1.

Initially we derive projected and deprojected cooling time profiles for these coarsely binned spectra in the same way as for the more finely binned spectra described in Sections 3.1 and 3.2. The coarse profiles match our original profiles albeit with higher "central" cooling time due to the higher altitude at which it is measured. Next, we refit the models for the more finely binned spectra but now keep the temperature fixed to that measured across the corresponding coarsely sampled region (i.e., we fix to the corresponding coarse temperature in the inner $\lesssim$40 kpc for each cluster). The normalization (hence density) is allowed to vary, thus we effectively simulate one method that can be used to push measurements of cooling profile to small radii in clusters with too few counts to finely trace the central temperature—specifically that of assuming a single temperature across the central regions. The resulting normalizations (alongside the fixed temperatures) are used to calculate "degraded" cooling time profiles. The percentage difference between our original cooling profiles and these "degraded" profiles is shown in Figure 4.

From Figure 4 we see that deviations in cooling time are typically <10% as a result of fixing a central temperature, though the error appears to increase toward smaller radii—as expected due to greater discrepancy here because the coarsely measured temperature is naturally dominated by emission at

higher altitudes within the central bin (here ∼20 kpc) as a result of geometry. Further, the effect is exacerbated after deprojection.

An alternative to fixing the inner temperature to a single value is to extrapolate the temperature profile to small radii and then fix to these extrapolated values. While preferable to a single fixed temperature, we can see by considering panel (a) of both Figures 1 and 2 that the inner temperature profiles of clusters are not necessarily amenable to robust extrapolation (see also Section 5). While density is the dominant driver of cooling time, we caution against overinterpretation of cooling profiles to small radii where projected or coarsely sampled temperatures have been combined with deprojected, more finely sampled densities.

3.4.1. A Further Word on Two-temperature Fitting

The same two-temperature models discussed in Section 3.3 were fitted to the coarsely binned spectra. A second temperature was not favored by the fits to A2199 or A85. Considering Figure 3, this is perhaps unsurprising—the cooler component is present only at $r \lesssim 3$ kpc in these systems, hence the ∼20 kpc coarse central bin is dominated by single-phase ICM. However, for both A496 and Hydra A, where Figure 3 shows the multiphase region to extend over a greater volume, a two-temperature model is recovered in both projection and now deprojection—thus confirming the previous lack of detection in the deprojected spectra as being due to the low number of counts in the separate finely binned regions (see Section 3.3).

For the projected spectra of Hydra A (A496) $kT_{\rm h} = 3.04^{+0.03}_{-0.03}$ ($2.97^{+0.07}_{-0.05}$) keV and $kT_{\rm c} = 0.84^{+0.15}_{-0.10}$ ($1.32^{+0.10}_{-0.09}$) keV with a ratio of normalizations of $N_{\rm h}/N_{\rm c} = 122$ (16), where subscripts h and c denote the hotter and cooler X-ray phases respectively. The corresponding values for the deprojected spectra are $kT_{\rm h} = 2.74^{+0.07}_{-0.07}$ ($2.53^{+0.05}_{-0.05}$) keV and $kT_{\rm c} = 0.77^{+0.10}_{-0.10}$ ($1.15^{+0.77}_{-0.85}$) keV with the ratio of normalizations being 84 (22).

Using $P \propto n_{\rm e} kT$ and assuming pressure equilibrium between the two X-ray phases, we have $kT_{\rm h}/kT_{\rm c} = n_{\rm c}/n_{\rm h}$. The cooler component should therefore be a factor of 3.6 (2.3) denser than the hot component in Hydra A (A496). A consistent ratio is found using either the projected or deprojected spectra in each case. The MEKAL normalization parameter is $N \propto n_{\rm e}^2 V$, which combined with mass $M \propto n_{\rm e} V$ gives $M_{\rm h}/M_{\rm c} = kT_{\rm h} N_{\rm h}/kT_{\rm c} N_{\rm c}$. It follows that the hotter component appears ∼450 (40) times more abundant than the cooler component in projection, or ∼300 (50) times more so after deprojection in Hydra A (A496). The greater dominance of the hot phase coupled to its flatter temperature profile in Hydra A compared to A496 likely explains the much higher fractional errors that arise when a single temperature is forced onto the central regions of A496 than when the same is applied to Hydra A (Figure 4).

That the errors introduced by splicing independently fitted temperatures and densities to create a cooling profile appear to be dependent on the presence and extent of a second temperature component, as well as on the slope of the temperature profile, again suggests that great care needs to be taken when attempting to push cooling measurements to small radii. The measured temperatures for the coarsely sampled hotter component in both Hydra A and A496 again agree within 1σ with those obtained from a single-temperature fit.

4. Mass Profiles

In this section we derive mass profiles for our clusters, which are subsequently used to calculate gravitational accelerations and free-fall times. We briefly outline a couple of approaches that were attempted, discussing their relative merits and shortcomings, before describing our adopted approach. We present our final derived mass profiles, with comparisons to tracers at other wavelengths and at a range of radii, in Figures 5 and 6.

4.1. NFW Profiles

On large scales the Navarro–Frenk–White (NFW) profile (Navarro et al. 1997) is found to be an accurate description of the total gravitating potential of galaxy clusters (e.g., Pointecouteau et al. 2005; Mandelbaum et al. 2006; Vikhlinin et al. 2006; Schmidt & Allen 2007). Following Main et al. (2015), we initially employed the cluster mass mixing model NFWMASS within the XSPEC package CLMASS (Nulsen et al. 2010) to fit NFW profiles to our chosen clusters. This model assumes that the X-ray-emitting gas is in hydrostatic equilibrium and that the cluster is spherically symmetric.

Although a single NFW profile provides a good fit to the global mass profiles of galaxy clusters, at small radii the NFW profile alone underestimates the masses inferred from stellar velocity dispersions in the central galaxy (e.g., Fisher et al. 1995; Lauer et al. 2014). An additional component, assumed to be mainly due to the stellar mass of the BCG, therefore needs to be accounted for when fitting to the observational data.

Assuming hydrostatic equilibrium, Voit & Donahue (2015) estimated free-fall times in the ACCEPT sample by fitting each cluster's pressure and temperature profiles, and invoking a velocity dispersion floor at $250\,{\rm km\,s^{-1}}$ to account for the BCG's stellar mass. A limitation of this approach is that it means all clusters tend toward the same acceleration profile in the central regions. In Voit et al. (2015) this method was updated to a two-component model consisting of an NFW profile and a singular isothermal sphere (SIS) with velocity dispersion of $250\,{\rm km\,s^{-1}}$. This updated approach allows for variation in the innermost mass profile, though only to the extent possible by varying the NFW component that is itself dominated by emission at large radii. The velocity dispersions of many BCGs can be much higher than $250\,{\rm km\,s^{-1}}$. For example, Lauer et al. (2014) measured stellar dispersions in all BCGs hosted by Abell clusters at $z \lesssim 0.08$ and reported only 24.4% (92/377) as having $\sigma < 250\,{\rm km\,s^{-1}}$, with some BCGs having much higher dispersions, such as $462 \pm 39\,{\rm km\,s^{-1}}$ in A193 and $451 \pm 10\,{\rm km\,s^{-1}}$ in A2716. Imposing a floor of $250\,{\rm km\,s^{-1}}$ will bias the inner mass high or low given the observed range. This therefore motivates us to assign an individually tailored inner mass profile to each cluster. The nearby sample of Lauer et al. (2014) aside, velocity dispersions in BCGs are in short supply, hence we desire a method to obtain knowledge of the inner mass distribution that is applicable to all observed clusters.

4.2. Beyond a Single NFW Potential

To attempt to directly fit the X-ray data for a second component in the mass profile, the NFWMASS models were extended to allow the inclusion of an additional potential

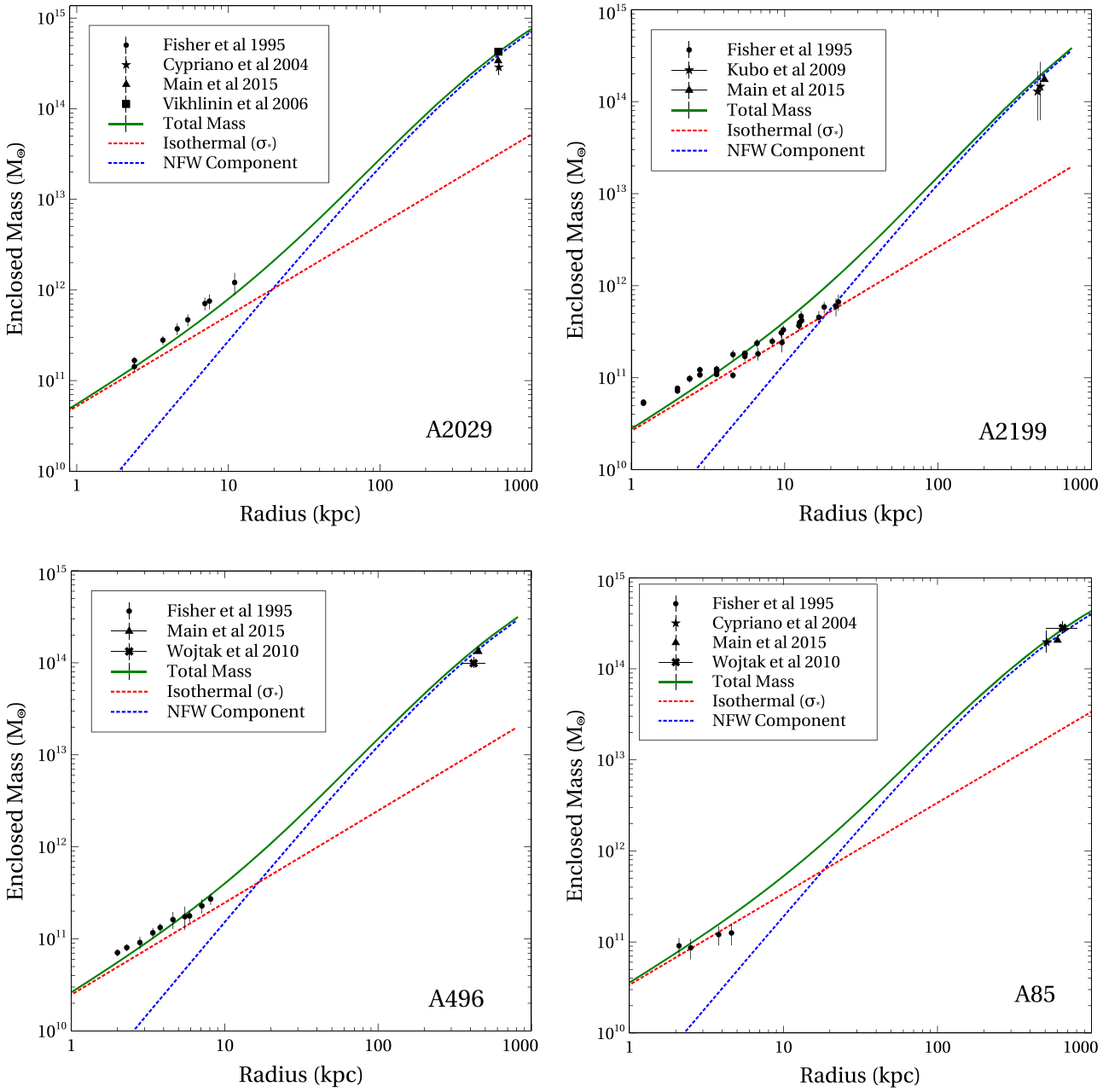

Figure 5. Mass profiles of the four objects for which Fisher et al. (1995) measured velocity dispersion profiles across the BCG. These profiles consist of an NFW component (blue) to account for the large-scale cluster potential and an isothermal component (red) to account for the stellar components in the inner regions. Agreement is seen both with the enclosed masses at small radii inferred from the observations of Fisher et al. (1995) and at large radii, where the profiles are compared to the M_{2500} values reported from a variety of sources that employed both X-ray (Vikhlinin et al. 2006; Allen et al. 2008; Main et al. 2015) and weak-lensing (Cypriano et al. 2004; Kubo et al. 2009) methods for mass estimation.

alongside the NFW potential

$$\Phi_{\rm NFW}(r) = -4\pi G\rho_0\, r_{\rm s}^2\, \frac{\ln(1+r/r_{\rm s})}{r/r_{\rm s}} \qquad (3)$$

where ρ_0 is the characteristic density and $r_{\rm s}$ the scale radius. Three options were considered for the second potential, with the resultant models dubbed NFWNFWMASS, ISONFWMASS, and HQNFWMASS. The NFWNFWMASS model simply had two concurrent NFW potentials with independent densities and scale radii. The HQNFWMASS and ISONFWMASS models consisted of an NFW profile combined with a Hernquist potential and an isothermal potential respectively. The Hernquist potential is

$$\Phi_{\rm H}(r) = -\frac{GM_{\rm H}}{r_{\rm H}}\frac{1}{1+r/r_{\rm H}} \qquad (4)$$

where $M_{\rm H}$ is the total mass assigned to this component and $r_{\rm H}$ is its scale radius. When a Hernquist profile is used to describe the stellar mass of the BCG this scale radius is $r_{\rm H} = r_{\rm e}/1.815$, where $r_{\rm e}$ is the effective radius of the BCG (Hernquist 1990). A basic isothermal sphere has potential $\Phi_{\rm iso}(r) = 2\sigma^2\ln(r)$, which can cause issues at $r = 0$. Instead, a modified cored

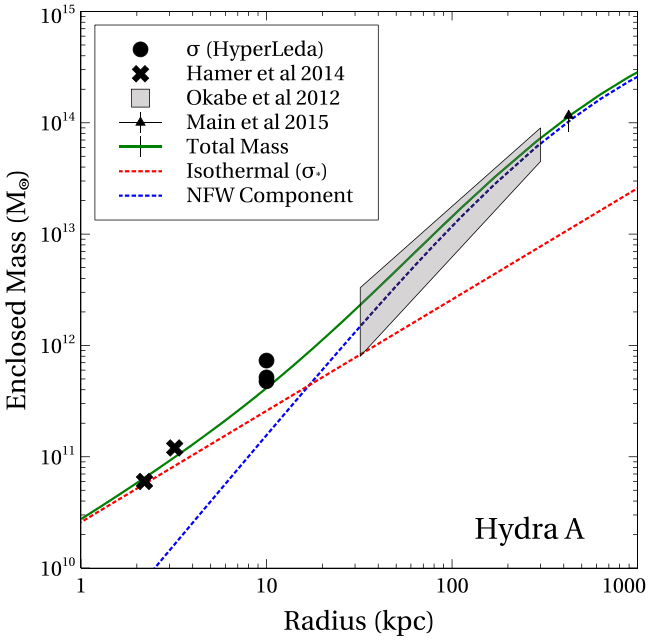

Figure 6. Mass profile for the Hydra A cluster. Our combined profile (green) consists of an NFW component (blue) to account for the large-scale cluster potential and an isothermal component (red) to account for the stellar component within the BCG. We achieve good agreement with the total cluster mass (M_{2500}) reported by Main et al. (2015) from their X-ray analysis, as well as with the mass profile of Okabe et al. (2015) derived from weak lensing. At smaller radii we see agreement with the dynamical masses inferred by Hamer et al. (2014) due to the presence of a large molecular gas reservoir. We additionally show the mass inferred from three velocity dispersion measurements reported in the HyperLEDA database. Note, however, that these velocity dispersions are reported without their aperture sizes, and hence a typical radius of 10 kpc was taken for plotting purposes.

isothermal potential is used:

$$\Phi_{\rm iso,c}(r) = \sigma^2 \ln(1 + (r/r_{\rm I})^2) \quad (5)$$

where $r_{\rm I}$ is a scale radius and σ the velocity dispersion. The core is a numerical requirement to prevent a singular central potential but can be used to account for the flattened stellar cores seen in many BCGs.

It was found that directly fitting two components to the X-ray data with these mixing models did not behave as hoped. The non-NFW component in the mass profiles is expected to be mainly attributable to the stellar mass content of the BCG. The resolution of *Chandra* coupled to the number of counts required per annulus for our mass modeling means that we only expect one or two annuli to contain an appreciable amount of this second component. Practically this meant that the mass profile was dominated by the single NFW component and that the second component was typically minimized, and only unstable solutions could be found. The NFWNFWMASS model in particular was found to be most unstable, with the similar potential seemingly vying for dominance, hence we removed this model from consideration.

4.3. Anchoring the BCG Stellar Component

Anchoring the second component to an observable that is available for all (or at least the vast majority of) BCGs whose clusters have been or are likely to be observed with *Chandra* is preferable, because this will allow an approach that can be applied homogeneously to a large sample. 2MASS (Skrutskie et al. 2006) covers essentially the full sky at the *J*, *H*, and *K* bands. The *K*-band (2.17 μm) extended source catalog is well suited to our needs since this wavelength is a good tracer of stellar light while not being overtly affected by AGN and dust emission.

It was highlighted by Lauer et al. (2007) that the relatively shallow survey depth of 2MASS means that the size of the extended envelopes known to exist around many BCGs is often underestimated, leading to both the total stellar mass and effective radii being similarly affected. A Hernquist component requires both of these latter parameters and hence would be highly uncertain if anchored from 2MASS data. Similar uncertainties arise at other wavelengths, hence we removed this model potential from consideration.

Away from its cored region, the SIS is defined entirely by a single velocity dispersion that is constant at all radii. We therefore utilize the isophotal radii ($r_{\rm K20}$) and apparent magnitudes ($m_{\rm K20}$) reported by 2MASS that are defined as the radius at which the surface brightness reaches 20 mag arcsec^{-2}. This isophotal magnitude should give us a reliable measurement of the light within a certain radius, which can be used to obtain an equivalent stellar velocity dispersion at the same radius. This $m_{\rm K20}$ was corrected for galactic extinction (Schlegel et al. 1998), as well as being evolution-corrected and *K*-corrected following Poggianti (1997). The stellar mass enclosed within $r_{\rm K20}$ is calculated using

$$\log \frac{M}{L_{\rm K}} = -0.206 + 0.135\,(B - V) \quad (6)$$

from Bell et al. (2003), who derived mass-to-light relations for a large mixed sample of galaxies. While isolated giant ellipticals are typically "red and dead," BCGs often display enhanced blueness due to ongoing low-level star formation (Rafferty et al. 2008), meaning that a mixed sample is reasonable. Equivalent relations for only BCGs were unavailable. We adopt a corrected $B-V$ color of 1.0 that is appropriate for massive BCGs (Baldry et al. 2008). Our derived stellar mass within $r_{\rm K20}$ was converted to a circular velocity and finally an equivalent stellar velocity dispersion using the relation

$$V_{\rm c} = (1.32 \pm 0.09)\sigma_* + (46 \pm 14) \quad (7)$$

from Pizzella et al. (2005), who derived this correlation using HI circular velocity measurements for a sample of elliptical galaxies.

This *equivalent stellar velocity dispersion* (σ_*) is not a measurable quantity—it is the inferred velocity dispersion that would be measured at $r_{\rm K20}$ if the BCG consisted only of its stars. The total halo mass of the cluster is believed to be well accounted for by the NFW profile. Self-similarity of dark-matter haloes suggests that the BCG itself should be considered the dominant galaxy within the cluster halo and is thus not expected to reside within its own dark-matter subhalo (e.g., George et al. 2012). Combining an NFW component and an isothermal sphere with velocity dispersion equal to our derived σ_* should result in a mass profile that accounts for the total cluster potential as well as the stellar mass of the BCG at the center.

To account for the mass of the fixed stellar component when fitting for the cluster NFW potential, we use the ISONFWMASS model with the isothermal normalization fixed to match our

Table 2
Details of the ISONFWMASS Profile Fits

Cluster	σ_* (km s^{-1})	$\rho_{0,\mathrm{ISO}}$ (keV)	$R_{s,\mathrm{NFW}}$ (arcmin)	$\rho_{0,\mathrm{NFW}}$ (keV)	R_{2500} (kpc)	M_{2500} ($\times 10^{14}\,M_\odot$)
A2029	335.9 ± 10.0	0.694	$6.79^{+0.49}_{-0.46}$	$88.68^{+4.84}_{-4.10}$	686.1	$4.94^{+0.17}_{-0.19}$
A2199	238.9 ± 4.0	0.351	$26.05^{+2.41}_{-3.07}$	$72.48^{+5.43}_{-6.82}$	558.1	$2.54^{+0.12}_{-0.18}$
A496	228.1 ± 4.6	0.320	$14.00^{+2.88}_{-2.09}$	$45.65^{+5.93}_{-3.68}$	482.5	$1.65^{+0.11}_{-0.11}$
A85	270.4 ± 6.4	0.450	$7.37^{+0.46}_{-0.21}$	$49.24^{+1.64}_{-0.92}$	516.7	$2.07^{+0.04}_{-0.03}$
Hydra A	236.6 ± 8.4	0.344	$5.85^{+0.53}_{-0.49}$	$32.29^{+1.52}_{-1.55}$	423.6	$1.14^{+0.03}_{-0.04}$

Note. Columns are: (i) cluster name, (ii) equivalent stellar velocity dispersion, (iii) isothermal potential $= \mu m_{\mathrm{H}} \sigma^2$ where m_{H} is the mass of the hydrogen atom and the mean atomic weight is $\mu = 0.59$, (iv) NFW scale radius, (v) NFW potential $= 4\pi G \rho_0 R_s^2 \mu M_{\mathrm{H}}$ in units of keV, (vi) R_{2500}, (vii) M_{2500}. The reported $\rho_{0,\mathrm{ISO}}$ values correspond to the σ_* values and were kept fixed in the fitting to account for the anchored stellar mass component. See text for more details.

derived σ_*. The r_{I} parameter (see Equation (5)) is set to an arbitrarily small but nonzero value ($\ll$1 kpc), ensuring that our cored isothermal component's potential is equivalent to a basic SIS[9] model at all radii of interest. Our input and fitted mass model parameters are listed in Table 2. Our derived equivalent velocity dispersions for this small sample range between 225 and 335 km s^{-1} (Table 2).

4.4. Comparison Mass Tracers

Our mass profiles are shown in Figures 5 (A2029, A2199, A496, A85) and 6 (Hydra A). To ensure that these profiles are reliable we require comparison mass tracers. All five of our clusters were modeled by Main et al. (2015), who obtained hydrostatic cluster mass estimates from their *Chandra* observations using the same CLMASS package of mixing models that we have used here. With the caveat that our data and methods are therefore not independent, we encouragingly find consistent total cluster masses (reported as M_{2500}) with these authors. Additionally, A2029 was included in the X-ray cluster analyses of both Vikhlinin et al. (2006) and Allen et al. (2008). We plot their M_{2500} values on Figure 5 and again find consistency.

X-ray-derived cluster masses can be in tension with other tracers, leading us to search for mass estimates obtained using different methods. Okabe et al. (2015) used weak-lensing analysis to derive an outer mass profile for Hydra A, which we show in Figure 6 to be in agreement with our X-ray measurements. This profile was in similar agreement with the X-ray mass profile of David et al. (2001). A2029 and A85 were included in the weak-lensing analysis of Cypriano et al. (2004). These authors approximated the cluster mass on large scales ($\gtrsim$arcmin) as an isothermal sphere and reported cluster velocity dispersions. Although an SIS is known to be a poor fit to cluster mass profiles across all radii (Schmidt & Allen 2007), this is a reasonable approximation at the scales of interest. We converted their velocity dispersions at R_{2500} to masses using the standard SIS potential: $\Phi_{\mathrm{iso}}(r) = 2\sigma^2 \ln(r)$. Kubo et al. (2009) used data from the Sloan Digital Sky Survey (Abazajian et al. 2009) to study weak-lensing signatures around seven nearby clusters, including A2199, for which they report an M_{200}. Our *Chandra* coverage does not extend to these altitudes and hence our profiles are highly uncertain if extrapolated so far (see Section 4.5.2). Instead, we use the assumption of Cypriano et al. (2004) that the cluster outskirts can be approximated as an SIS to convert this M_{200} to an M_{2500}. As an additional test of the uncertainty of this extrapolation we adopt the 363.0 kpc NFW scale radius of Main et al. (2015) for this cluster and vary the normalization to match the M_{200} reported in Kubo et al. (2009) with an NFW profile, from which we then read an equivalent M_{2500}. These two M_{2500} values are consistent, in addition to being in agreement with our derived mass profile. Although a mass estimate from weak lensing could not be found for A496, this cluster does appear in the sample of clusters to which Wojtak & Łokas (2010) fitted mass profiles using the dynamics of the constituent galaxies. All of these weak-lensing and dynamical total cluster mass estimates are shown on Figure 5 and found to be in agreement with our mass profiles.

The five clusters within this paper were selected as having tracers of their inner mass profiles at various radii. For Hydra A these come from the integral field unit (IFU) observations of cold gas motions in the central galaxy presented by Hamer et al. (2014). We also find three stellar velocity dispersions (Heckman et al. 1985) reported in the HyperLEDA database (Makarov et al. 2014) for the central galaxy in the Hydra A cluster, which we convert to mass estimates and plot at a representative 10 kpc. The remaining four clusters all have stellar velocity dispersion profiles featured in Fisher et al. (1995), which we convert to estimates of gravitating mass using Equation (7) and plot on Figure 5. One caveat is that converting stellar velocity dispersion profiles to inferred masses assumes an isotropic distribution with minimal net flow. Ordered, and disordered but anisotropic, stellar motions within the BCGs can therefore bias the resultant inferred masses. Indeed, rotating Hα gas clouds are seen in some BCGs (Hamer et al. 2016) so it is perhaps not unreasonable to expect some degree of ordered motion also in the stellar component. However, we note that Fisher et al. (1995) measured very little rotation in their sample of 13 BCGs. It is also known from IFU surveys that among ellipticals there is an anticorrelation between mass and rotational support, with all "non-rotators" in the SAURON survey having $M > 10^{11.25}\,M_\odot$ (Emsellem et al. 2007). Furthermore, while not all slow rotators are massive, all massive galaxies tend to be slow rotators (Emsellem et al. 2011). Effectively this means that BCGs are almost always "non-rotators" or "slow rotators." Additionally, Loubser et al. (2008) measured the anisotropy parameter (Kormendy 1982) as a function of luminosity and showed that BCGs are even less rotationally supported than field giant

[9] Interestingly it was found that the basic SIS model matched the low-altitude mass tracers better than a cored isothermal model with the core radius set to match the stellar core radius. We speculate that this may suggest that at the smallest radii ($\leqslant$2 kpc) the mass of the supermassive black hole starts to become important to the total mass (see also Kelson et al. 2002), but this is beyond the scope of this work.

ellipticals, which as a class already show very low levels of rotation. The evidence therefore suggests that stellar velocity dispersions are a reasonable mass proxy for BCGs at the centers of galaxy clusters.

4.4.1. Comparison of Shape

While the NFW profile is widely believed to accurately trace the gravitating mass of clusters on large scales (e.g., Pointecouteau et al. 2005; Mandelbaum et al. 2006; Zappacosta et al. 2006; Schmidt & Allen 2007), the situation is less clear at small radii. In a fairly recent paper Newman et al. (2013a) used a combination of strong lensing, weak lensing, and stellar kinematics to calculate mass profiles spanning $r \sim 3$–3000 kpc for seven clusters at $z = 0.2$–0.3. They found that a generalized-NFW (gNFW) profile could provide a good fit to the total mass down to small radii, giving a total density slope in the range $0.003 < r/r_{200} < 0.03$ ($\sim$5–53 kpc) that is consistent with that of simulated dark-matter-only NFWs. A steeply increasing stellar component at small radii makes this consistent with their earlier work that found the dark-matter-only component to have a central density profile much shallower than an NFW one (Sand et al. 2002, 2004, 2008; Newman et al. 2011).

In a sister paper to Newman et al. (2013a), the same authors used lensing and dynamics to separate the dark matter and stellar contributions in their mass profiles, finding the stellar component to become dominant below $\sim$5–10 kpc (Newman et al. 2013b). This is in contrast to our derived profiles, where the isothermal component intended to account for stellar mass becomes dominant at $\sim$15–20 kpc. We note that our higher crossover radii are comparable to typical effective radii of BCGs (e.g., Hoessel et al. 1987) and that Gavazzi et al. (2007) found that the transition from dark matter to stellar dominance in the mass profiles of normal ellipticals occurs around $R_{\rm eff}$. However, as we discuss in Section 4.5.2, not truncating the isothermal component has the effect of increasing the NFW scale radius. This means that part of the halo mass at intermediate radii ($\sim$10–30 kpc) is effectively accounted for within the isothermal component. The radius at which our isothermal and NFW components cross is therefore model-dependent, hence not directly comparable to that of Newman et al. (2013a). Furthermore the gNFWs used by Newman et al. (2013a) allow the inner density slope to vary from that of the simple NFW profile that we use, which may also account for some of the discrepancy.

We stress that although the isothermal and NFW components can broadly be considered capable of accounting for the stellar and dark matter (+gas) components of our clusters, they are not exactly so, and caution should be employed in interpreting them as such. Ultimately our aim is to calculate total mass profiles that reliably match ancillary data. Though we have no sample overlap with Newman et al. (2013a) our profile shapes are qualitatively similar, being described by an NFW profile down to 5–20 kpc and having a stellar component become increasingly important below this. Overall we find good agreement between our calculated mass profiles and comparison tracers at both large and small radii, thus showing our technique to be a feasible approach for tracing cluster mass profiles down into the central galaxy using only freely available X-ray and NIR data.

4.5. Estimating Uncertainties

4.5.1. Random Statistical Errors

Error estimation within XSPEC itself defaults to Gaussian statistics. The parameters describing the NFW scale radius (*nfwa*) and potential (*nfwpot*) in the mass mixing models (see Nulsen et al. 2010) are co-dependent and hence this approach will give unreliable uncertainties. Instead, to estimate errors on these we create a Markov chain Monte Carlo (MCMC) chain of 5000 iterations, which is used to obtain the reported 1σ errors (see Table 2). Uncertainties on the 2MASS magnitudes are propagated through to σ_* and a similar MCMC chain of 5000 iterations is then created for the isothermal component. Uncertainties on M_{2500}, and at each step of the mass profiles, are estimated by running 5000 combinations of these chains.

4.5.2. Systematic Error Consideration

A potential systematic effect in our adopted approach concerns the isothermal component continuing to increase to large radii ($\geqslant$20 kpc), beyond where we would reasonably expect the stars of the BCG to form a significant contribution to the total mass budget. This problem could be alleviated by truncating the isothermal component's mass with a sharp cut at some radius, although this approach is rejected because it would introduce an unphysical discontinuity in the density and associated mass profiles. Alternatively a maximum mass could be assigned to the isothermal component, and a damping term included so that the profile asymptotes to this maximum mass rather than having a sharp discontinuity. However, this approach suffers from the issue that damping the isothermal component would cause the resultant mass at $r_{\rm K20}$ to be less than our calculated stellar mass at that radius. Furthermore, a physically motivated maximum mass and damping radius would have to be associated with the highly uncertain BCG effective radii $R_{\rm e}$.

The mass distribution associated with the NFW potential (Equation (3)) is

$$M(r) = 4\pi\rho_0 r_{\rm s}^3 \left[\ln\left(1 + \frac{r}{r_{\rm s}}\right) - \frac{r/r_{\rm s}}{1 + r/r_{\rm s}}\right] \quad (8)$$

where $r_{\rm s}$ is the scale radius. At large r ($r \gg r_{\rm s}$) the NFW component's mass therefore varies proportionally to $\ln(r/r_{\rm s}) - 1$. For the singular isothermal sphere potential $2\sigma^2 \ln(r/r_{\rm l})$, the mass distribution $= 2\sigma^2 r/G$. Hence at sufficiently large radii, the non-truncated isothermal component will always dominate the logarithmic NFW mass distribution. However, the radial range that we are interested in is typically less than a few NFW scale radii and so our analysis is less affected by this effect. At radii below the NFW scale radius this component's mass distribution increases more quickly than that of the isothermal component at the same radii.

The problem of the isothermal component existing in our fits beyond where the stars dominate is mitigated because the mass associated with the NFW component rises much faster over the radial range in which we are interested than the mass associated with the isothermal component. Indeed, this latter component contributes an increasingly smaller fraction of the mass budget toward the largest radii that we trace our mass profiles to. Nevertheless, although the ISONFWMASS model with fixed isothermal component finds the optimized NFW component to

provide the best-fit total mass profile, having an artificially inflated contribution from the isothermal component that becomes fractionally less important at larger radii could affect the shape of our final mass profiles. Practically this means less mass is "free" at smaller radii to be fitted with the NFW profile. Accordingly, the NFW scale radius R_s is pushed to larger values so that the NFW mass contribution is lessened toward the center, while the normalization is increased to recover the total mass at larger radii. This effect is likely to subtly change the shape of the final mass profile, potentially most prevalently at the intermediate radii (between a few tens and a few hundred kiloparsecs) where lower-entropy core gas is postulated to be lifted and become unstable in the stimulated feedback model.

We can quantify this effect by looking at the fractional difference with radius between the final mass profiles from our ISONFWMASS fits and a comparison mass profile consisting of a fitted NFW profile coupled with an isothermal component truncated at some radius. To obtain these comparison profiles we first measure the isothermal component's mass at 10 kpc for each cluster. We then insert this central mass as a fixed constant, and fit an NFW profile to account for the remaining (majority) mass in each cluster. Note that the central region ($\lesssim$10 kpc) is excluded in each of these comparison fits. The comparison profiles therefore consist of the isothermal component truncated at 10 kpc, coupled with the NFW component that was fitted outside this radius but accounting for this constant central mass. The resulting profiles are therefore effectively produced similarly to our ISONFWMASS fits but with an artificially truncated isothermal component—an approach that was earlier rejected since it introduces an unphysical mass discontinuity at the truncation radius. Nevertheless, this approach is suitable for our current investigation of the systematic effect of a non-truncated isothermal component.

The percentage difference between these profiles and our final ISONFWMASS profiles, defined as

$$\text{Difference} = 100 \times \left(1 - \frac{M_{\text{comparison}}}{M_{\text{ISONFWMASS}}}\right), \quad (9)$$

is shown in Figure 7. Each of the ratios in this plot tells the same tale. The ISONFWMASS and comparison profiles converge toward $r = 0$ as the NFW component becomes increasingly negligible. Below $\sim$10 kpc the ISONFWMASS fit gives less mass, which is consistent with it tending to have a higher NFW scale radius and thus a smaller NFW contribution at smaller radii. A sharp transition is seen at $\approx$10 kpc where the isothermal component in the comparison profiles is artificially truncated. We reiterate that the isothermal component's truncated mass is still accounted for in the comparison profile at all radii, just as a fixed mass beyond the truncation radius. The sharp transition is because the isothermal component still constitutes a large fraction of the total mass at $\sim$10 kpc. The ISONFWMASS model therefore continues to rise at almost the same rate beyond the truncation radius, whereas the comparison profile barely increases at radii just above $r \sim 10$ kpc, causing a sharp (but not instant) transition from negative to positive values in Figure 7. The NFW component rises more quickly than the isothermal component at radii much less than the NFW scale radius. However, at $\sim$20–40 kpc the ISONFWMASS profile gives slightly higher mass because its still rising isothermal component continues to contribute an

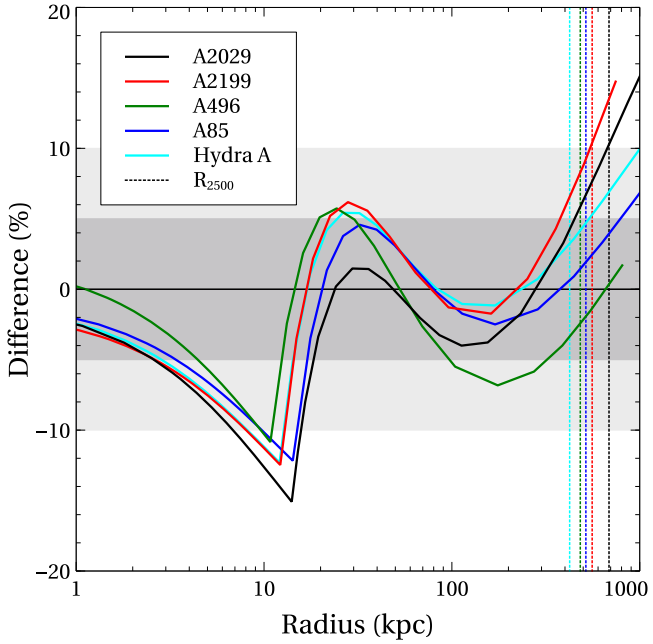

Figure 7. Percentage difference (see Equation (9)) in mass between our ISONFWMASS profiles and a singular NFW fit where a constant mass equivalent to the isothermal component at 10 kpc is accounted for in fitting. The vertical dotted lines correspond to the R_{2500} for each color-coded cluster. We see that systematic differences in the resultant mass profiles are $\lesssim$10% out to at least R_{2500}, beyond which the fits diverge. The sharp transition at $r \approx 10$ kpc is due to the artificial truncation of the isothermal component in the singular NFW fit. For a full description see Section 4.5.2.

appreciable fraction of the mass budget. At radii $\gtrsim$40 kpc the NFW component begins to dominate the mass budget. Between $\sim$40 and 300 kpc the larger NFW scale radius in the ISONFWMASS fits means that this model's mass prediction is systematically lower than that of the comparison. Finally, the lower scale radius of the comparison model causes its mass profile to flatten at $\sim$300 kpc whereas the ISONFWMASS continues to rise, causing the profiles to diverge. The different mass scalings of the NFW and isothermal components at large r, as discussed near the beginning of this section, will cause this divergence to grow to yet larger radii.

There are clearly systematic uncertainties associated with the inclusion of a non-truncated isothermal component. However, these result in only around $\lesssim$10% difference in the mass profiles out to at least R_{2500}. The free-fall time is $t_{\text{ff}} \propto M^{-1/2}$, hence this effect is further lessened. Our derived profiles are therefore believed to be robust to at least this accuracy below R_{2500}, although we caution that extrapolation of our fits to greater radii than this is likely to be uncertain.

4.6. The Importance of Defining the Cluster Center

A major motivation of our work is to understand the role of mass in maintaining the balance between heating and cooling in cluster cores. As previously mentioned, recent simulations have suggested that one important facet of this may be a cooling instability that triggers hot gas to condense at some threshold value of $t_{\text{cool}}/t_{\text{ff}}$ (e.g., McCourt et al. 2012; Sharma et al. 2012; Gaspari et al. 2013; Li et al. 2015; Prasad et al. 2015). Observationally testing such a threshold is challenging. In Section 3.4 we investigated the effect of resolution on measured t_{cool}. Being able to trace the mass, and associated

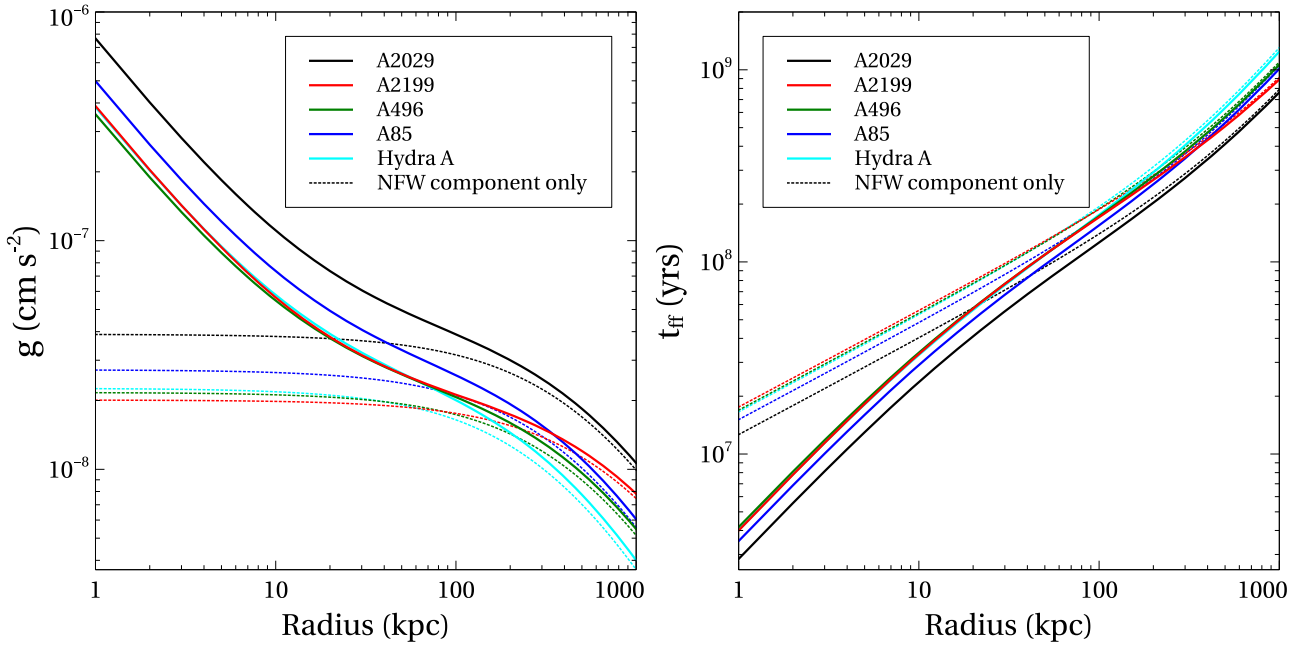

Figure 8. Radial run of acceleration (left) and free-fall time (right) corresponding to the mass profiles derived in Section 5. Shown as dotted lines are the equivalent parameters when the additional isothermal mass component associated with the BCG is neglected. The acceleration felt by cold gas clumps in cluster centers, as seen by ALMA, is highly dependent upon their distance from the central galaxy, with implications for the mechanisms required to retard the velocities of these clouds within the stimulated feedback model. Note also that the discrepancy of a factor of 2–5 in free-fall time when the isothermal component is neglected is similarly dependent upon radial distance from the assigned center, highlighting the importance of the choice of cluster center in the ultimate measurement of $(t_{\rm cool}/t_{\rm ff})_{\rm min}$.

parameters such as acceleration and free-fall time, to small radii is similarly crucial in being able to test these models.

A common approximation for the free-fall time (e.g., McDonald et al. 2015; Voit et al. 2015), defined with respect to local gravitational acceleration g, is

$$t_{\rm ff} = \sqrt{\frac{2r}{g}}. \quad (10)$$

We adopt this definition of the free-fall time for our profiles in order that they are easily comparable to the literature.

Figure 8 shows the radial run of accelerations and free-fall times corresponding to the mass profiles derived in the previous section. Also shown are the equivalent parameters if the isothermal component of the mass is neglected (i.e., for the cluster NFW component only). The accelerations associated with these NFW-only mass profiles are in good agreement with the NFW-only acceleration profile derived for PKS0745-191 in Sanders et al. (2014). However, consideration of Figures 5 and 6 shows the requirement to account for the BCG, with Figure 8 highlighting that the calculated gravitational acceleration can otherwise be underestimated by more than an order of magnitude.

The importance of the assigned cluster center is apparent when considering the right-hand panel of Figure 8, even among this small exploratory sample. There is a factor of 2–5 difference in inferred free-fall time between the NFW-only component and the total mass component. As the free-fall time is dependent upon distance from the center, the choice of dynamical center can have a large effect on the ultimate minimum value of, for example, $t_{\rm cool}/t_{\rm ff}$ that is measured.

Defining the center of a cluster is an imperfect art. Even the assertion that there is a center to be defined implies a degree of symmetry that is not always present. However, the importance of this latter point is mitigated here since the most disturbed clusters are by and large those with long central cooling times. A difference of a factor of a few in $t_{\rm cool}/t_{\rm ff}$ is therefore less important since for these clusters cooling is not seen and the measured $t_{\rm cool}/t_{\rm ff}$ is usually at least an order of magnitude above any postulated cooling thresholds (e.g., Voit et al. 2015). Conversely, the clusters where cooling is expected to occur have not recently experienced major disturbance, and the assumption of spherical symmetry is typically reasonable, especially on large scales. Nonetheless, as seen from Figure 8 a miscentering by only $\sim$10 kpc could greatly affect $t_{\rm cool}/t_{\rm ff}$.

Multiple definitions exist for the cluster center. Perhaps the most natural is the peak of the cluster potential, as is often defined in simulations. Similarly, lensing mass measurements use reconstructive methods to infer the mass distribution, with the center typically taken as the potential peak. However, often this has large errors due to intrinsic galaxy shapes and cluster substructure where even small centroid offsets can cause cluster mass to be underestimated by $\sim$30% (George et al. 2012).

With X-ray data the two most natural choices of center are the X-ray centroid and the X-ray peak. Usually, but not always, these indicators are in close agreement (e.g., Mann & Ebeling 2012). Another natural choice for the cluster centroid is the middle of the BCG. Although not all clusters contain a BCG, the vast majority of cool-core clusters do. Furthermore, these BCGs are typically located close ($\lesssim$50 kpc) to the X-ray peak and/or centroid (e.g., Lin & Mohr 2004; Mann & Ebeling 2012; Rozo & Rykoff 2014; von der Linden et al. 2014). Indeed, studying a sample of 129 massive groups, George et al. (2012) found the massive galaxy closest ($\leqslant$75 kpc) to the X-ray centroid (i.e., the BCG) to be the best tracer of dynamical center out of eight tracers considered, a result supported by the simulations of Cui et al. (2015). In a sample of 19 clusters, Loubser et al. (2016) found that the four with BCGs located within a projected 5 kpc of the X-ray

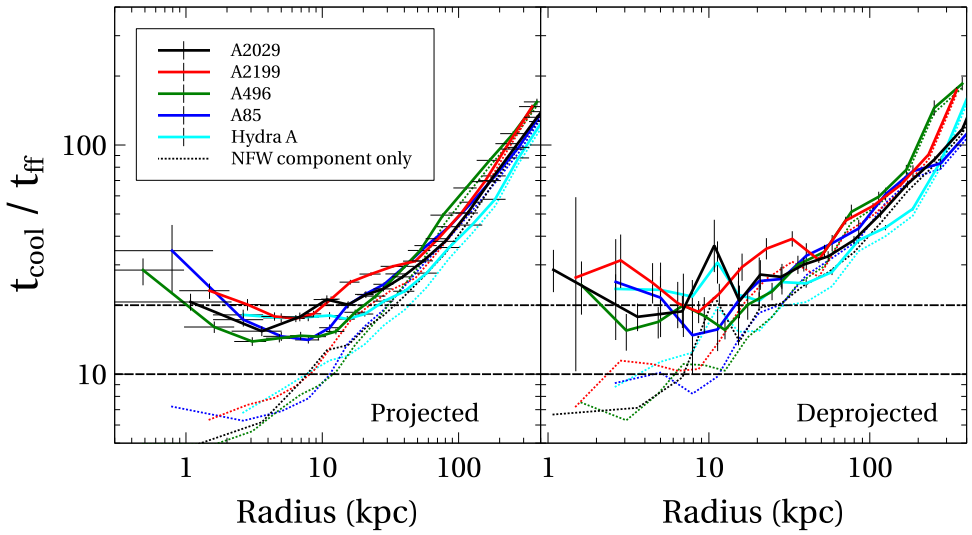

Figure 9. Projected (left) and deprojected (right) t_{cool}/t_{ff} profiles for our evaluation sample. Dotted lines on both panels show the equivalent parameters if the isothermal mass component associated with the BCG is neglected. Horizontal error bars in the left panel reflect bin width. The same bin widths are used in the right panel but are not shown. Minimum values of t_{cool}/t_{ff} lie in the range 14.8–21.8 for our deprojected profiles.

centroid were the only BCGs in their sample with appreciable ongoing star formation.

Returning to the left panel of Figure 8, the acceleration associated with the NFW component of our mass distribution is seen to be relatively flat inward of about 100 kpc. This is due to the r^{-2} dependence of the gravitational acceleration being counteracted by the slope of the NFW density approaching an r^{-1} scaling well within the scale radius such that $M \propto r^2$. The effect of the galaxy itself (seen via the isothermal component) is most potent at radii <10 kpc. The cooling instability models are concerned primarily with gas condensing from the hot phase and ultimately fuelling AGN feedback (e.g., McCourt et al. 2012; Sharma et al. 2012; Prasad et al. 2015). That the BCGs in cool-core clusters are found to be typically <50 kpc from the cluster center, and that the local gravity associated with the cluster halo on these scales is less dependent on position than gravity associated with the BCG itself, therefore compels us to take the center of the BCG as the most appropriate centroid for our study. This choice is further supported by the distribution of molecular gas seen with ALMA, which is found to lie near the BCG and be associated with X-ray cavities that are directly associated with it (e.g., McNamara et al. 2014; Russell et al. 2014, 2016; Tremblay et al. 2016).

We note retrospectively that such a criterion was used for each of the clusters in this current study, where in each case a very clear BCG exists in close association with the X-ray centroid (see also Section 2.2.1). However, in non-cool-core clusters the identification of a BCG is often uncertain, and the more diffuse X-ray atmosphere has a less well defined centroid. In all cases for the larger sample we therefore suggest that the cluster center be assigned a ranked centering grade. For clusters with a clearly dominant optical/IR BCG that resides close to the X-ray centroid the center of this galaxy should be assigned as cluster center. In clusters with no clear BCG then the X-ray centroid itself is taken to be the cluster center, with the closest major galaxy classified as the BCG. The inclusion of an isothermal component to account for this "BCG" would overestimate the mass in the inner regions of these clusters—thus where no central BCG is present a velocity dispersion of zero is appropriate, and the fits revert to a single NFW component.

5. Discussion

5.1. Early Comparison to Precipitation Models

One of our main motivations is to understand AGN feedback as a function of mass (Main et al. 2015). Accurate mass profiles that extend down into cluster centers are important because the processes governing gas cooling within cluster cores are believed to be underpinned by dependence on the cluster mass. For example, it has long been known (e.g., Cowie et al. 1980; Nulsen 1986) that gas becomes thermally unstable when t_{cool}/t_{ff} falls to unity. More recently, precipitation models suggest that gas condensation from the hot phase may occur below a threshold value of $t_{cool}/t_{ff} \sim 10$ (e.g., McCourt et al. 2012; Sharma et al. 2012; Gaspari et al. 2013; Prasad et al. 2015). Previous studies (e.g Gaspari et al. 2012; Voit et al. 2015) found that t_{cool}/t_{ff} profiles reach a minimum value at ~5–20 kpc before increasing at yet smaller radii. Again this highlights the importance of accurately determining the central mass profiles and having deprojected density and temperature measurements down to small radii.

A full discussion of gas cooling in cluster cores in the context of the precipitation and stimulated feedback models is beyond the scope of this paper and therefore left to upcoming work with a larger cluster sample. However, as a proof of concept Figure 9 shows the projected and deprojected t_{cool}/t_{ff} ratios for our exploratory sample. Note that a 10% systematic mass uncertainty (Section 4.5.2) is factored into our calculations of the error in free-fall time. Among our small sample we find minimum values of t_{cool}/t_{ff} that span the range 14.8–21.8 (Figure 9). Though a direct comparison for these specific clusters is not possible, our minimum values are consistent with the range reported by Voit et al. (2015), who found most clusters to have t_{cool}/t_{ff} minima between ~10 and 20. However, with the caveat that our sample is small, we see no indication of any t_{cool}/t_{ff} minima falling below 10 (as in Voit & Donahue 2015), in possible tension with precipitation models. It is worth noting that the unusual cluster A2029, which falls

below the thresholds for both cooling time and entropy, but fails to exhibit Hα, does not stand out in this sample, with $(t_{\rm cool}/t_{\rm ff})_{\rm min} = 17.8$. In the stimulated feedback model (McNamara et al. 2016) this is attributed to A2029's inability to lift low-entropy gas from the core to an altitude at which gas stability is breached.

Also shown in Figure 9 are the $t_{\rm cool}/t_{\rm ff}$ profiles found when the BCG (i.e., the isothermal component) is neglected. It is evident that both the minimum value of $t_{\rm cool}/t_{\rm ff}$ and the radius where it is found are dictated by the BCG. Deriving an accurate central mass profile (and subsequently $t_{\rm cool}/t_{\rm ff}$) therefore requires a measurement of the central galaxy's mass that is tailored to each individual cluster, as is done in the technique described within this paper.

5.2. Resolution Effects and Possible Implications for Lack of Extended Isentropic Cores in Cool-core Clusters

In Figure 9 the minimum values of $t_{\rm cool}/t_{\rm ff}$ are clearly well sampled radially. However, as discussed in Section 3.4, limited angular resolution can often lower the accuracy to which central cluster properties can be determined. As a test, we can use our coarsely binned spectra from Section 3.4 to simulate the effect that lower spatial resolution would have on the measured minimum values of $t_{\rm cool}/t_{\rm ff}$ displayed in Figure 9. Such lower spatial resolution could arise due to clusters being located at higher redshift, or alternatively be due to shallower data requiring that larger central annuli be used to obtain enough X-ray counts so that deprojected models can successfully be fitted. We calculated $t_{\rm cool}/t_{\rm ff}$ profiles for our coarsely binned spectra (see Section 3.4) and in all cases found that the measured deprojected (projected) $t_{\rm cool}/t_{\rm ff}$ minima were a factor of 2.6–9.4 (2.0–6.4) higher than when finer sampling was used. We stress that factors of two or more in this ratio are important within the context of thermal instability and precipitation models. Ensuring that quantities measured from observations are as accurate as possible is therefore crucial for comparison to simulations. In conjunction with our finding in Section 3.4 that extrapolation of cooling profiles becomes uncertain below the radii at which temperature can be directly measured, the most accurate $t_{\rm cool}/t_{\rm ff}$ investigations can therefore only be performed on clusters whose central $\sim$5–20 kpc are well sampled, corresponding to $z \lesssim 0.6$ with *Chandra*. Count rates will of course restrict this range further in practice.

A final point that can be illustrated using Figure 9, and also Figure 2, is the importance of deriving fully deprojected cluster properties such as density, and in particular temperature, down to small radii. As discussed in Section 3.2, our deprojected entropy profiles do not show any suggestion of flattening toward an isentropic "entropy floor." Instead our central entropies appear to be best described by a split power law, and continue to drop below $\sim$10 keV cm^2 rather than becoming isentropic in the core.

Using different cluster samples, Panagoulia et al. (2014) and Lakhchaura et al. (2016) both reported that the central entropies among their low-entropy clusters (i.e., strong cool-core clusters) were lower than the equivalent central entropies in the ACCEPT database (Cavagnolo et al. 2009). The former of these authors used a "progressive subtraction of outer envelope" deprojection similar to that used within this work (e.g., DSDEPROJ), whereas the latter used an MCMC technique to jointly fit X-ray spectra across a range of radii. Lakhchaura et al. (2016) claimed that the ACCEPT profiles combined projected temperatures with higher resolution deprojected densities, and concluded that the higher temperatures therefore cause the higher central entropy. However, it should be highlighted that Cavagnolo et al. (2009) actually performed two different treatments of the central temperature and published two different inner entropy profiles for each cluster (see Table 5 of Cavagnolo et al. 2009). The first method was to assume a constant central temperature across a central region (as we investigated in Section 3.4), whereas the second used a linear temperature gradient extrapolated from the measurements at higher altitudes. The values presented in the online ACCEPT database to which Panagoulia et al. (2014) and Lakhchaura et al. (2016) appear to have compared their results use only the former of these temperature treatments.

Table 3
Comparison of Our Innermost Measured Entropies to those of the ACCEPT Database (Cavagnolo et al. 2009)

Cluster	Innermost K (keV cm^{-2})		
	This work	ACCEPT- c.T.	ACCEPT- e.T.
A85	$11.6^{+3.8}_{-2.3}$	16.3 ± 0.5	11.8 ± 0.5
A496	$4.8^{+0.7}_{-0.6}$	10.5 ± 0.6	6.4 ± 0.6
A2029	$6.6^{+1.0}_{-0.7}$	16.5 ± 0.4	13.1 ± 0.4
A2199	$3.7^{+1.1}_{-1.5}$	13.9 ± 0.6	8.6 ± 0.6
Hydra A	$8.8^{+1.1}_{-0.9}$	16.9 ± 0.7	16.5 ± 0.7

Note. Columns are: (i) cluster name, (ii) our innermost entropy value, (iii) innermost entropy value from ACCEPT assuming a constant inner temperature, (iv) innermost entropy value from ACCEPT when temperature was extrapolated from the fit at larger radii. Note that the central radius of the bin in which the central entropy values were calculated agrees to with 0.1 kpc for those in our analysis and the equivalent values from ACCEPT, except for A2029 where our central bin is centered at 1.1 kpc compared to 3.4 kpc for ACCEPT. A more appropriate comparison for this cluster is to use our second innermost entropy measurement of $13.2^{+1.2}_{-1.1}$ keV cm^2 in a bin centered at 3.6 kpc, which we note shows good agreement with the minimum ACCEPT value when an extrapolated temperature is used. Note that the values presented in the online ACCEPT database use the method of a constant central temperature.

In Table 3 we compare our innermost entropy values to the equivalent values from the ACCEPT database (Cavagnolo et al. 2009), using both the constant and extrapolated temperature methods. We see that, similar to what was found by Lakhchaura et al. (2016) and Panagoulia et al. (2014), our innermost entropy values lie below the equivalent numbers in the ACCEPT database when a constant central temperature is assumed. The degree of discrepancy varies markedly among our small sample, from a deficit of only about 20% below the ACCEPT value in A2029 (when the comparison is made with our second innermost entropy value—see caption of Table 3) to a deficit of roughly 73% in A2199. Better agreement is found with the entropy values that are calculated using an extrapolated temperature, though our innermost entropies are still on average around 26% lower, with a range of 0%–57% among this small exploratory sample. As reported previously, the differences seen due to the different methods for extracting inner entropy measurements could result in the difference between entropy profiles that appear to flatten in the core (and so become isentropic) and ones that continue to fall as they reach altitudes less than 1 kpc.

The five clusters studied within this paper were specifically chosen for their deep *Chandra* data. Data of equivalent depth are unavailable for most clusters, so alternative approaches to direct deprojection of temperature are sometimes necessary when dealing with larger samples. However, we are now finding that a broken power law is the best fit to the entropy profiles in a larger sample of cool-core clusters, which will be published in an upcoming paper (M. T. Hogan et al. 2017, in preparation). The analysis here suggests that fitting the innermost temperature profile and extrapolating inward is a more robust approach than using a constant temperature when studying the inner entropy profiles of cool-core clusters, though even this approach should be employed with caution.

6. Conclusions

In this paper we have used a small exploratory sample of clusters with deep *Chandra* observations and ancillary mass measurements to develop a method for determining mass distribution across a wide radial range. Additionally, we have considered a number of potential observational effects that could impact measurements of cooling properties in galaxy clusters. In particular we find that:

1. Mass distributions can be well modeled by a combination of a singular isothermal sphere component anchored to the stellar mass of the BCG, and an NFW profile fitted to the X-ray data. The effect of the isothermal component continuing to large radii gives $\lesssim$10% uncertainty on the final mass profile out to M_{2500}.
2. Our entropy profiles are best described by a broken power law, which at large radii appears to follow the baseline $K \propto r^{1.1}$ scaling expected from gravity alone (Tozzi & Norman 2001; Voit et al. 2005) and at lower radii follows a $K \propto r^{0.67}$ scaling as seen in Panagoulia et al. (2014). We exclude large isentropic cores in these clusters down to our resolution limit ($\sim$1 kpc).
3. We argue that, for clusters containing an obvious central BCG, the BCG represents the best location for the cluster center.
4. Tentative evidence suggests that the cooler component in a two-temperature thermal model fit to central ICM may be associated with extended nebular emission. A single-temperature fit is found to be adequate to trace cooling of the hot phase down to $\sim$1 kpc.
5. The central regions of galaxy clusters ($r \lesssim 20$ kpc) are poorly modeled by a constant temperature. Fixing temperature within the inner $\sim$20 kpc leads to errors of approximately 10% on cooling time, which increase at small radii.
6. None of our exploratory sample has $t_{\rm cool}/t_{\rm ff}$ below 10, although four out of five exhibit Hα emission indicative of ongoing cooling.

The techniques described within this paper are to be applied to a larger sample of clusters to further investigate thermal instability and AGN feedback within galaxy clusters from an observational viewpoint in upcoming papers (M. T. Hogan et al. 2017, in preparation; F. Pulido et al. 2017, in preparation).

Support for this work was provided in part by the National Aeronautics and Space Administration through *Chandra* Award Number G05-16134X issued by the *Chandra* X-ray Observatory Center. M.T.H., B.R.M., A.N.V., and F.P. acknowledge support from the Natural Sciences and Engineering Research Council of Canada. H.R.R. acknowledges support from ERC Advanced Grant Feedback 340442. We also wish to thank the referee, Mark Voit, for his helpful comments that have improved the clarity of this paper. The scientific results reported in this article are based on observations made by the *Chandra X-ray Observatory* and have made use of software provided by the *Chandra* X-ray Center (CXC) in the application packages CIAO, ChIPS, and Sherpa. The plots in this paper were created using Veusz.

References

Abazajian, K. N., Adelman-McCarthy, J. K., Agüeros, M. A., et al. 2009, ApJS, 182, 543
Hitomi Collaboration, Aharonian, F., Akamatsu, H., et al. 2016, Natur, 535, 117
Allen, S. W., Evrard, A. E., & Mantz, A. B. 2011, ARA&A, 49, 409
Allen, S. W., Rapetti, D. A., Schmidt, R. W., et al. 2008, MNRAS, 383, 879
Arnaud, K. A. 1996, in ASP Conf. Ser. 101, Astronomical Data Analysis Software and Systems V, ed. G. H. Jacoby & J. Barnes (San Francisco, CA: ASP), 17
Baldry, I. K., Glazebrook, K., & Driver, S. P. 2008, MNRAS, 388, 945
Balucinska-Church, M., & McCammon, D. 1992, ApJ, 400, 699
Bell, E. F., McIntosh, D. H., Katz, N., & Weinberg, M. D. 2003, ApJS, 149, 289
Biffi, V., Borgani, S., Murante, G., et al. 2016, arXiv:1606.02293
Blanton, E. 2016, Natur, 535, 40
Bleem, L. E., Stalder, B., de Haan, T., et al. 2015, ApJS, 216, 27
Boehringer, H., & Morfill, G. E. 1988, ApJ, 330, 609
Cavagnolo, K. W., Donahue, M., Voit, G. M., & Sun, M. 2008, ApJL, 683, L107
Cavagnolo, K. W., Donahue, M., Voit, G. M., & Sun, M. 2009, ApJS, 182, 12
Churazov, E., Brüggen, M., Kaiser, C. R., Böhringer, H., & Forman, W. 2001, ApJ, 554, 261
Churazov, E., Tremaine, S., Forman, W., et al. 2010, MNRAS, 404, 1165
Cowie, L. L., Fabian, A. C., & Nulsen, P. E. J. 1980, MNRAS, 191, 399
Crawford, C. S., Allen, S. W., Ebeling, H., Edge, A. C., & Fabian, A. C. 1999, MNRAS, 306, 857
Cui, W., Power, C., Biffi, V., et al. 2015, arXiv:1512.01253
Cypriano, E. S., Sodré, L., Jr., Kneib, J.-P., & Campusano, L. E. 2004, ApJ, 613, 95
David, L. P., Jones, C., & Forman, W. 1996, ApJ, 473, 692
David, L. P., Nulsen, P. E. J., McNamara, B. R., et al. 2001, ApJ, 557, 546
de Plaa, J., Zhuravleva, I., Werner, N., et al. 2012, A&A, 539, A34
Donahue, M., Horner, D. J., Cavagnolo, K. W., & Voit, G. M. 2006, ApJ, 643, 730
Edge, A. C. 2001, MNRAS, 328, 762
Emsellem, E., Cappellari, M., Krajnović, D., et al. 2007, MNRAS, 379, 401
Emsellem, E., Cappellari, M., Krajnović, D., et al. 2011, MNRAS, 414, 888
Fabian, A. C. 1994, ARA&A, 32, 277
Fabian, A. C. 2012, ARA&A, 50, 455
Fabian, A. C., Sanders, J. S., Crawford, C. S., et al. 2003, MNRAS, 344, L48
Fabian, A. C., Sanders, J. S., Ettori, S., et al. 2000, MNRAS, 318, L65
Fisher, D., Illingworth, G., & Franx, M. 1995, ApJ, 438, 539
Freeman, P. E., Kashyap, V., Rosner, R., & Lamb, D. Q. 2002, ApJS, 138, 185
Fruscione, A., McDowell, J. C., Allen, G. E., et al. 2006, Proc. SPIE, 6270, 62701V
Gaspari, M., Ruszkowski, M., & Oh, S. P. 2013, MNRAS, 432, 3401
Gaspari, M., Ruszkowski, M., & Sharma, P. 2012, ApJ, 746, 94
Gaspari, M., Temi, P., & Brighenti, F. 2016, arXiv:1608.08216
Gavazzi, R., Treu, T., Rhodes, J. D., et al. 2007, ApJ, 667, 176
George, M. R., Leauthaud, A., Bundy, K., et al. 2012, ApJ, 757, 2
Hamer, S. L., Edge, A. C., Swinbank, A. M., et al. 2014, MNRAS, 437, 862
Hamer, S. L., Edge, A. C., Swinbank, A. M., et al. 2016, arXiv:1603.03047
Heckman, T. M., Illingworth, G. D., Miley, G. K., & van Breugel, W. J. M. 1985, ApJ, 299, 41
Hernquist, L. 1990, ApJ, 356, 359
Hillel, S., & Soker, N. 2016a, MNRAS, 455, 2139
Hillel, S., & Soker, N. 2016b, arXiv:1608.07818
Hoekstra, H., Bartelmann, M., Dahle, H., et al. 2013, SSRv, 177, 75
Hoekstra, H., Herbonnet, R., Muzzin, A., et al. 2015, MNRAS, 449, 685
Hoessel, J. G., Oegerle, W. R., & Schneider, D. P. 1987, AJ, 94, 1111
Kalberla, P. M. W., Burton, W. B., Hartmann, D., et al. 2005, A&A, 440, 775
Kelson, D. D., Zabludoff, A. I., Williams, K. A., et al. 2002, ApJ, 576, 720

Kitayama, T., Bautz, M., Markevitch, M., et al. 2014, arXiv:1412.1176
Kormendy, J. 1982, in Morphology and Dynamics of Galaxies, Proc. Twelfth Advanced Course (Sauverny: Observatoire de Genève) pp. 113 (A84-15502 04-90)
Kravtsov, A. V., & Borgani, S. 2012, ARA&A, 50, 353
Kubo, J. M., Annis, J., Hardin, F. M., et al. 2009, ApJL, 702, L110
Lakhchaura, K., Deep Saini, T., & Sharma, P. 2016, arXiv:1601.02347
Lauer, T. R., Faber, S. M., Richstone, D., et al. 2007, ApJ, 662, 808
Lauer, T. R., Postman, M., Strauss, M. A., Graves, G. J., & Chisari, N. E. 2014, ApJ, 797, 82
Li, Y., Bryan, G. L., Ruszkowski, M., et al. 2015, ApJ, 811, 73
Liedahl, D. A., Osterheld, A. L., & Goldstein, W. H. 1995, ApJL, 438, L115
Lin, Y.-T., & Mohr, J. J. 2004, ApJ, 617, 879
Loubser, S. I., Babul, A., Hoekstra, H., et al. 2016, MNRAS, 456, 1565
Loubser, S. I., Sansom, A. E., Sánchez-Blázquez, P., Soechting, I. K., & Bromage, G. E. 2008, MNRAS, 391, 1009
Main, R., McNamara, B., Nulsen, P., Russell, H., & Vantyghem, A. 2015, arXiv:1510.07046
Makarov, D., Prugniel, P., Terekhova, N., Courtois, H., & Vauglin, I. 2014, A&A, 570, A13
Mandelbaum, R. 2015, JInst, 10, C05017
Mandelbaum, R., Seljak, U., Cool, R. J., et al. 2006, MNRAS, 372, 758
Mann, A. W., & Ebeling, H. 2012, MNRAS, 420, 2120
McCourt, M., Sharma, P., Quataert, E., & Parrish, I. J. 2012, MNRAS, 419, 3319
McDonald, M., McNamara, B. R., van Weeren, R. J., et al. 2015, ApJ, 811, 111
McDonald, M., Veilleux, S., Rupke, D. S. N., & Mushotzky, R. 2010, ApJ, 721, 1262
McNamara, B. R., & Nulsen, P. E. J. 2007, ARA&A, 45, 117
McNamara, B. R., & Nulsen, P. E. J. 2012, NJPh, 14, 055023
McNamara, B. R., Russell, H. R., Nulsen, P. E. J., et al. 2014, ApJ, 785, 44
McNamara, B. R., Russell, H. R., Nulsen, P. E. J., et al. 2016, arXiv:1604.04629
Mewe, R., Gronenschild, E. H. B. M., & van den Oord, G. H. J. 1985, A&AS, 62, 197
Mewe, R., Lemen, J. R., & van den Oord, G. H. J. 1986, A&AS, 65, 511
Nagai, D., Vikhlinin, A., & Kravtsov, A. V. 2007, ApJ, 655, 98
Navarro, J. F., Frenk, C. S., & White, S. D. M. 1997, ApJ, 490, 493
Nelson, K., Lau, E. T., & Nagai, D. 2014, ApJ, 792, 25
Newman, A. B., Treu, T., Ellis, R. S., & Sand, D. J. 2011, ApJL, 728, L39
Newman, A. B., Treu, T., Ellis, R. S., & Sand, D. J. 2013b, ApJ, 765, 25
Newman, A. B., Treu, T., Ellis, R. S., et al. 2013a, ApJ, 765, 24
Nulsen, P. E. J. 1986, MNRAS, 221, 377
Nulsen, P. E. J., Powell, S. L., & Vikhlinin, A. 2010, ApJ, 722, 55
O'Dea, C. P., Baum, S. A., Privon, G., et al. 2008, ApJ, 681, 1035
Okabe, N., Umetsu, K., Tamura, T., et al. 2015, arXiv:1503.04412
Panagoulia, E. K., Fabian, A. C., & Sanders, J. S. 2013, MNRAS, 433, 3290
Panagoulia, E. K., Fabian, A. C., & Sanders, J. S. 2014, MNRAS, 438, 2341
Peterson, J. R., Kahn, S. M., Paerels, F. B. S., et al. 2003, ApJ, 590, 207
Pizzella, A., Corsini, E. M., Dalla Bontà, E., et al. 2005, ApJ, 631, 785
Plagge, T., Benson, B. A., Ade, P. A. R., et al. 2010, ApJ, 716, 1118
Planck Collaboration, Ade, P. A. R., Aghanim, N., et al. 2015, A&A, 581, A14
Poggianti, B. M. 1997, A&AS, 122 arXiv:astro-ph/9608029
Pointecouteau, E., Arnaud, M., & Pratt, G. W. 2005, A&A, 435, 1
Ponman, T. J., Sanderson, A. J. R., & Finoguenov, A. 2003, MNRAS, 343, 331
Prasad, D., Sharma, P., & Babul, A. 2015, ApJ, 811, 108
Rafferty, D. A., McNamara, B. R., & Nulsen, P. E. J. 2008, ApJ, 687, 899
Romanowsky, A. J., & Kochanek, C. S. 2001, ApJ, 553, 722
Rozo, E., & Rykoff, E. S. 2014, ApJ, 783, 80
Russell, H. R., Fabian, A. C., McNamara, B. R., & Broderick, A. E. 2015, MNRAS, 451, 588
Russell, H. R., McNamara, B. R., Edge, A. C., et al. 2014, ApJ, 784, 78
Russell, H. R., McNamara, B. R., Fabian, A. C., et al. 2016, MNRAS, arXiv:1602.05962
Russell, H. R., Sanders, J. S., & Fabian, A. C. 2008, MNRAS, 390, 1207
Salomé, P., & Combes, F. 2003, A&A, 412, 657
Sand, D. J., Treu, T., & Ellis, R. S. 2002, ApJL, 574, L129
Sand, D. J., Treu, T., Ellis, R. S., Smith, G. P., & Kneib, J.-P. 2008, ApJ, 674, 711
Sand, D. J., Treu, T., Smith, G. P., & Ellis, R. S. 2004, ApJ, 604, 88
Sanders, J. S., & Fabian, A. C. 2002, MNRAS, 331, 273
Sanders, J. S., & Fabian, A. C. 2007, MNRAS, 381, 1381
Sanders, J. S., & Fabian, A. C. 2008, MNRAS, 390, L93
Sanders, J. S., & Fabian, A. C. 2011, MNRAS, 412, L35
Sanders, J. S., Fabian, A. C., Hlavacek-Larrondo, J., et al. 2014, MNRAS, 444, 1497
Sanderson, A. J. R., Edge, A. C., & Smith, G. P. 2009, MNRAS, 398, 1698
Schlegel, D. J., Finkbeiner, D. P., & Davis, M. 1998, ApJ, 500, 525
Schmidt, R. W., & Allen, S. W. 2007, MNRAS, 379, 209
Sharma, P., McCourt, M., Quataert, E., & Parrish, I. J. 2012, MNRAS, 420, 3174
Skrutskie, M. F., Cutri, R. M., Stiening, R., et al. 2006, AJ, 131, 1163
Soker, N. 2016, NewAR, 75, 1
Sparks, W. B., Donahue, M., Jordán, A., Ferrarese, L., & Côté, P. 2004, ApJ, 607, 294
Takahashi, T., Mitsuda, K., Kelley, R., et al. 2010, Proc. SPIE, 7732, 77320Z
Tozzi, P., & Norman, C. 2001, ApJ, 546, 63
Tremblay, G. R., O'Dea, C. P., Baum, S. A., et al. 2015, MNRAS, 451, 3768
Tremblay, G. R., Oonk, J. B. R., Combes, F., et al. 2016, Natur, 534, 218
Vantyghem, A. N., McNamara, B. R., Russell, H. R., et al. 2014, MNRAS, 442, 3192
Vantyghem, A. N., McNamara, B. R., Russell, H. R., et al. 2016, arXiv:1610.00716
Vikhlinin, A., Kravtsov, A., Forman, W., et al. 2006, ApJ, 640, 691
Voit, G. M., & Donahue, M. 2015, ApJL, 799, L1
Voit, G. M., Donahue, M., Bryan, G. L., & McDonald, M. 2015, Natur, 519, 203
Voit, G. M., Kay, S. T., & Bryan, G. L. 2005, MNRAS, 364, 909
Voit, G. M., Meece, G., Li, Y., et al. 2016, arXiv:1607.02212
von der Linden, A., Allen, M. T., Applegate, D. E., et al. 2014, MNRAS, 439, 2
Werner, N., Oonk, J. B. R., Canning, R. E. A., et al. 2013, ApJ, 767, 153
Werner, N., Zhuravleva, I., Churazov, E., et al. 2009, MNRAS, 398, 23
Witze, A. 2016, Natur, 533, 18
Wojtak, R., & Łokas, E. L. 2010, MNRAS, 408, 2442
Yang, H.-Y. K., & Reynolds, C. S. 2016, ApJ, 829, 90
Zappacosta, L., Buote, D. A., Gastaldello, F., et al. 2006, ApJ, 650, 777